

RESEARCH ARTICLE

10.1029/2019JE006178

Key Points:

- Constraints on continuous and time-varying atmospheric pressure are derived from preserved, ancient crater populations
- Crater chronology functions are used to constrain accumulation time for crater populations at different atmospheric pressures
- Existing paleopressure data are most consistent with low atmospheric pressures early in Mars' history

Supporting Information:

- Supporting Information S1

Correspondence to:

A. O. Warren,
aowarren@uchicago.edu

Citation:

Warren, A. O., Kite, E. S., Williams, J.-P., & Horgan, B. (2019). Through the thick and thin: New constraints on Mars paleopressure history 3.8–4 Ga from small exhumed craters. *Journal of Geophysical Research: Planets*, 124. <https://doi.org/10.1029/2019JE006178>

Received 19 AUG 2019

Accepted 5 OCT 2019

Author Contributions

Conceptualization: A. O. Warren, E. S. Kite

Data curation: E. S. Kite

Funding Acquisition: E. S. Kite

Methodology: E. S. Kite, J.-P. Williams

Software: A. O. Warren, E. S. Kite, J.-P. Williams

Writing - Original Draft: A. O. Warren

Formal Analysis: A. O. Warren

Investigation: A. O. Warren

Project Administration: E. S. Kite

Resources: E. S. Kite, J.-P. Williams, B. Horgan

Supervision: E. S. Kite

Visualization: A. O. Warren

Writing - review & editing: E. S. Kite, J.-P. Williams, B. Horgan

Through the Thick and Thin: New Constraints on Mars Paleopressure History 3.8–4 Ga from Small Exhumed Craters

A. O. Warren¹ , E. S. Kite¹ , J.-P. Williams² , and B. Horgan³ 

¹Department of Geophysical Sciences, University of Chicago, Chicago, IL, USA, ²Department of Earth, Planetary and Space Sciences, University of California at Los Angeles, Los Angeles, CA, USA, ³Department of Earth, Atmospheric, and Planetary Sciences, Purdue University, West Lafayette, IN, USA

Abstract Mars' climate history depends in part on its atmospheric pressure evolution, but most existing constraints on atmospheric pressure are indirect. Thin atmospheres allow small objects to reach the surface and form impact craters; therefore, ancient impact craters can constrain past atmospheric pressure. To identify ancient craters preserved in sedimentary rocks and exhumed by wind erosion, we use HiRISE orthoimages, anaglyphs, and digital terrain models (DTMs). We compare measured crater populations from two sites to predictions from an atmosphere-impactor interaction model for atmospheres of different pressures. Our upper limits on continuous atmospheric pressure are 1.9 ± 0.1 bar around 4 Ga and 1.5 ± 0.1 bar at 3.8 ± 0.2 Ga. We demonstrate that atmospheric pressure cannot have been continuously above these upper limits. During the interval 3.8 ± 0.2 Ga, our crater counts require that atmospheric pressure was less than 5% of Earth's modern pressure for at least 10^4 yrs, or at higher pressure for a correspondingly longer duration of time (at least $10^5 - 10^6$ years at 1.5 bar for our Mawrth phyllosilicates and Meridiani Planum data, respectively). Therefore, atmospheric pressure around 4 Ga was either continuously 1.9 ± 0.1 bar or varied between higher (> 1.9 bar) and lower (< 1.9 bar) pressures. Similarly, atmospheric pressure at 3.8 ± 0.2 Ga was either continuously 1.5 ± 0.1 bar, or varied between higher (> 1.5 bar) and lower (< 1.5 bar) pressures. Finally, we synthesize all available paleopressure estimates for early Mars to constrain a 2-component model of Mars' long-term atmospheric pressure evolution. In our model, atmospheric pressures < 1 bar early in Mars' history best fit existing paleopressure constraints.

Plain Language Summary Atmospheric pressure helps control Mars' climate over time. Ancient impact craters give us upper limits on past atmospheric pressure. If atmospheric pressure is high, objects travel through a thicker, denser atmosphere. This stops more small objects from reaching the ground and forming craters. A group of ancient craters with lots of small craters indicates low atmospheric pressure during crater accumulation. We compare the proportion of small, ancient craters at 2 sites on Mars to models of craters for different atmospheres. This gives an upper limit of 1.9 bar around 4 billion years ago and 1.5 bar at 3.8 ± 0.2 billion years ago. It is possible that our observed craters formed while atmospheric pressure was changing. To form the groups of craters at our study sites, Mars' atmospheric pressure could either have been less than 5% of Earth's modern pressure for at least 10,000 years or could have been at higher pressure for a longer duration of time. We combine our new pressure results with other limits on Mars' past atmospheric pressure to model how Mars' atmospheric pressure has evolved over the last 4.4 billion years. Models where Mars' atmospheric pressure starts low fit existing data best.

1. Introduction

Changes in Mars' atmospheric pressure over time are an important control on climate evolution. Today, Mars' annual mean atmospheric pressure is 6 mbar. At these low atmospheric pressures, liquid water is not stable because it will boil at 273 K and is frozen at lower temperatures (Murphy & Koop, 2005). However, during the Late Noachian (3.84–3.7 Ga) and Early Hesperian (3.7–3.4 Ga), there is abundant geologic evidence for liquid water on the surface of Mars including fluvial landforms (e.g., Mangold et al., 2008; Moore et al., 2003), lake deposits (e.g., Fassett & Head, 2005; Grotzinger et al., 2014), and potentially a hemispheric ocean (e.g., Citron et al., 2018; di Achille & Hynek, 2010; Oehler & Allen, 2012). There is further evidence that the water that fed these lakes and channels was precipitation-derived (Ansan & Mangold, 2006;

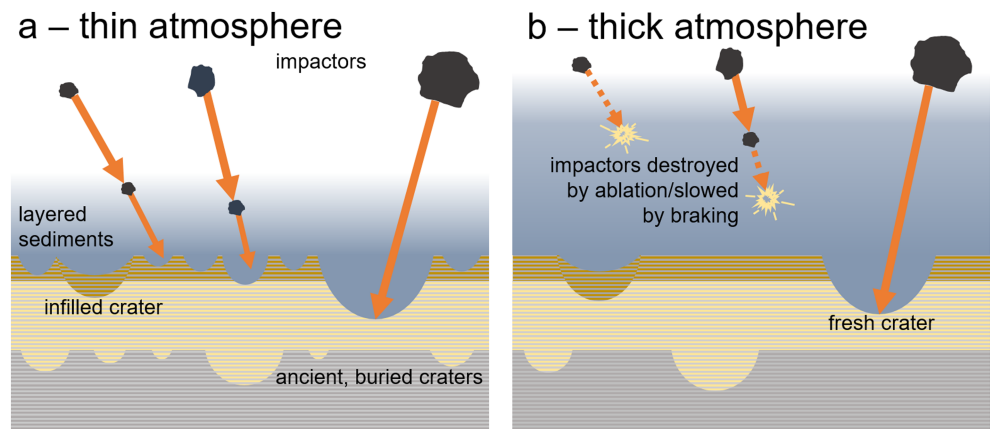


Figure 1. Schematic illustration of cratering due to impactors passing through a) a thin atmosphere, b) a thick atmosphere, also showing infill of ancient craters by layered sediments (example labelled “infilled crater”). The thin atmosphere case has a much higher proportion of smaller craters than the thick atmosphere case.

Hynek et al., 2010; Mangold et al., 2004). This implies that surface temperatures must have at least transiently reached 273 K. Another important control on the stability of water at the Martian surface is evaporitic cooling (Hecht, 2002), which efficiently removes heat from ice that would otherwise melt at 273 K, particularly at low atmospheric pressures, for example, on the present day Martian surface. To achieve the required elevated surface temperatures, models of early Mars climate invoke greenhouse warming by thick (≥ 1 bar), CO_2 atmospheres with some water vapor content (e.g., Haberle, 1998; Wordsworth et al., 2013, 2015) or CO_2 atmospheres with some fraction of H_2 , SO_2 , or CH_4 (e.g., Halevy & Head, 2014; Kite et al., 2017; Ramirez et al., 2014; Batalha et al., 2015; Wordsworth et al., 2017). Paleopressure estimates throughout Martian history are therefore important for constraining the maximum pressure of the atmosphere available at any given time for greenhouse warming.

One simple upper limit on Martian atmospheric pressure is the pressure at which CO_2 condenses into surface ice. The threshold pressure for this process depends on the minimum temperature anywhere on Mars' surface. In turn, the location of the coldest point on the surface depends on the atmospheric pressure. At low atmospheric pressures (e.g., ~ 6 mbar at the present day), surface temperature is predominantly controlled by latitude (e.g., Fastook & Head, 2015; Wordsworth et al., 2013). At high atmospheric pressures (> 1 bar), surface temperature is controlled by elevation. Using the relationship between temperature, elevation and latitude from Fastook and Head (2015) for an obliquity of 25° , we can estimate the minimum temperature on the Martian surface (assuming mostly elevation control of temperature in a > 1 bar atmosphere) during the deposition of sedimentary rocks on Mars. These sedimentary rocks form by the accumulation of loose material (e.g., sand/dust derived from erosion of existing rocks and ash from volcanic eruptions) and later cementation (hardening through mineral precipitation between grains Grotzinger & Milliken, 2012; Malin & Edgett, 2000). In this paper, we focus on sites on Mars where the exposed ancient sedimentary rocks must have formed in the presence of surface liquid water. The hydrous minerals observed at Mawrth Vallis require seasonal *surface* temperatures of at least 273 K to form (Bishop & Rampe, 2016), possibly approaching 300 K (Bishop et al., 2018). If Mawrth Vallis is assumed to be at an annual average temperature of 273 K, this gives a minimum annual average temperature at the South Pole of ~ 240 K. At this temperature, ~ 12 bar of CO_2 would need to exist for condensation into ice caps to occur (Bryson et al., 1974; Fernández-Fassnacht & Rio, 1984). We can apply the same approach to the sinuous ridge observed at our Meridiani site (interpreted to be an inverted channel by Davis et al., 2016). Observations from the Antarctic McMurdo Dry Valleys suggest that 255 K is close to the lowest annual average temperature at which fluvial processes can occur (Head & Marchant, 2014; Doran et al., 2010; Marchant & Head, 2007). Assuming an annual average temperature of 255 K at Meridiani, this gives a minimum annual average temperature of 225 K at the coldest point on Mars, which would require a ~ 7 bar CO_2 atmosphere for condensation to occur. Here we present results for each site that lower these upper limits on atmospheric pressure by a factor of 5.

To make a direct estimate of atmospheric pressure during crater accumulation, we can use ancient crater populations embedded in Martian stratigraphy (Kite et al., 2014). The minimum size of an impactor that can

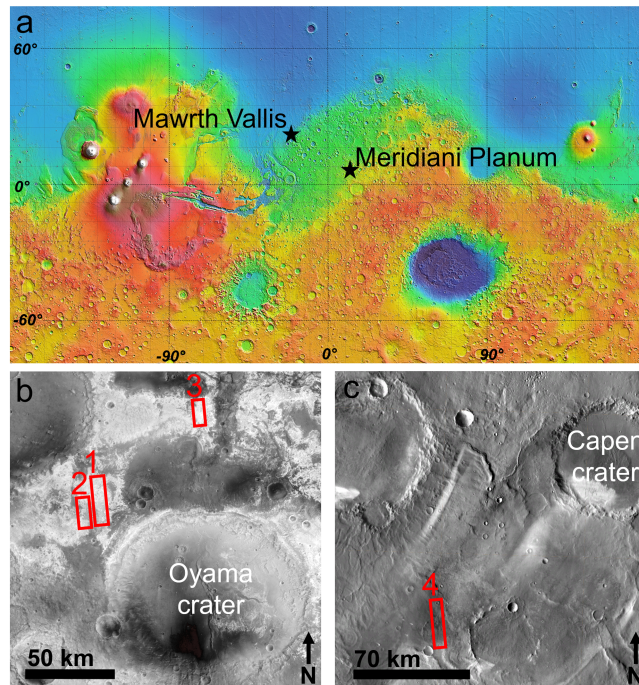


Figure 2. a) Global map of Mars showing locations of Mawrth Vallis and Meridiani Planum sites from this study and Aeolis Dorsa site from Kite et al. (2014) (Image credit: MOLA science team. Color scale shows elevation relative to Mars geoid overlain on shaded relief. Purple (e.g., 35°S 55°W) corresponds to −8 km, white (e.g., 10°S 120°E) corresponds to 8 km, b) HRSC Mawrth Vallis mosaic showing Mawrth HiRISE DTM locations (image credit: ESA/DLR/FU Berlin), c) THEMIS daytime IR mosaic showing Meridiani Planum HiRISE DTM location (image credit: NASA/USGS, ESA/DLR/FU Berlin). Numbering corresponds to location numbers (#) in Table 1.

reach the planetary surface and form a hypervelocity impact crater (Tauber & Kirk, 1976) is determined by the thickness and density of the atmosphere. In a thinner atmosphere, a greater proportion of smaller objects will be able to reach the surface travelling at high velocities, producing more small impact craters (Figure 1). Therefore, for the same impactor population, different atmospheric pressures will produce different crater size frequency distributions (CSFDs) (Figure 1). For craters embedded in ancient Martian sedimentary rocks, the ratio of small to large craters records atmospheric pressure during deposition. We use a model of atmosphere-impactor interactions (Williams et al., 2014) to generate synthetic crater populations for different atmospheric pressures. We fit measured CSFDs from craters preserved in ancient sedimentary units to the model-predicted CSFDs to find upper limits on continuous atmospheric pressure during the accumulation of crater populations preserved in ancient sedimentary rocks in Mawrth Vallis and Meridiani Planum. In contrast to existing indirect paleopressure constraints from thermodynamic studies of mineral stability at the Martian surface (Bristow et al., 2017; Hu et al., 2015; van Berk et al., 2012), our upper limit is insensitive to atmospheric composition and surface temperature. This is important because all recent modeling studies demonstrate that it is not possible to warm early Mars to 273 K with a pure CO₂ atmosphere (e.g., Forget et al., 2013; Wordsworth et al., 2013). A single site (e.g., Kite et al., 2014) is sufficient to get a global estimate of past atmospheric pressure. However, finding paleopressure estimates for sites of multiple ages gives us better temporal coverage of Martian atmospheric pressure evolution. By considering the effect of different geologic processes on crater populations we establish two end-member atmospheric pressure scenarios that are consistent with our measured CSFDs. To investigate Mars' paleopressure history as a whole, we integrate our new upper limits on continuous atmospheric pressure with existing paleopressure estimates and use these to constrain a basic, 2-component model of Mars' atmospheric pressure evolution. Our model results highlight where new data are needed and motivate the search for new Martian paleopressure estimates, particularly between 3.6 Ga and present.

The remainder of this paper is organized as follows. Section 2 will describe the geological context of the sedimentary units that preserve the ancient crater populations we are interested in. Section 3 will describe our criteria for crater identification and give a brief summary of our chosen atmosphere-impactor interaction

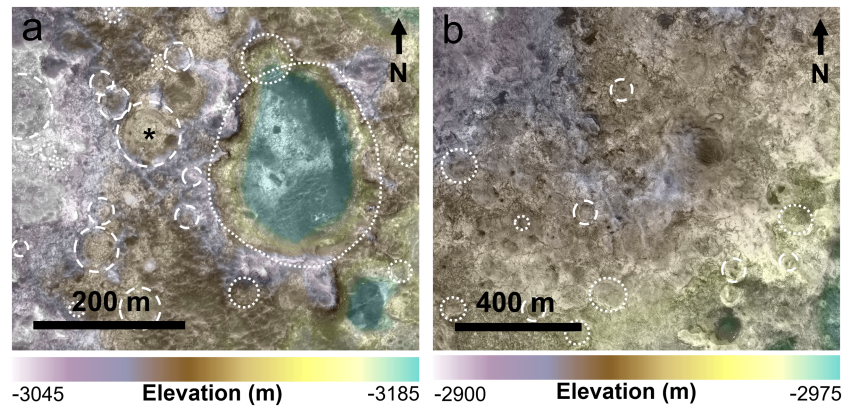


Figure 3. Examples of ancient craters in the two main units in our Mawrth Vallis site: (a) “Dark paleosurface” (image #1, crater with black asterisk in center shown in Figure 5), (b) phyllosilicates (image #2, dark-bottomed crater in bottom left (near letter m) centered at 21–12′ 52.89°W, 24–30′ 50.53°N). Dashed ellipses outline exhumed ancient craters. Dotted ellipses outline candidate exhumed craters that are not included in our final ancient crater counts.

model (Williams et al., 2014). Section 4 will summarize the results from fitting model-predicted CSFDs to our measured CSFDs and states our new upper limits on *constant* atmospheric pressure. Section 5 will discuss processes that can modify CSFDs, the effect of *time-varying* atmospheric pressure, and demonstrates that our results are globally representative upper limits on continuous atmospheric pressure. Section 6 will summarize our conclusions.

2. Geological Context

2.1. Mawrth Phyllosilicates

The Noachian phyllosilicates north/northwest of Oyama crater (24.5°N, 21.0°W, Figure 2b, “Mawrth” herein) are composed of thick units (>150 m; Loizeau et al., 2007) of little-deformed (Michalski et al., 2010), finely layered sedimentary deposits. Hydrous clay minerals (Bishop et al., 2008) make these phyllosilicates of interest for constraining the atmospheric pressure during the Early Noachian (4.10–3.95 Ga), when liquid water must have been present for alteration to occur. These minerals suggest that surface temperatures must have been at least 273 K according to Bishop and Rampe (2016), but may have been as high as 310 K (Bishop et al., 2018). Additionally, the Mawrth phyllosilicates overlie a dark paleosurface (Loizeau et al., 2010, Figure 3a), which traps an even more ancient crater population. These craters are infilled with layered phyllosilicates and therefore must predate the main phyllosilicate deposition (Loizeau et al., 2012). The preservation of >100-m diameter craters on this paleosurface shows that it was exposed long enough to be impacted by bolides (Loizeau et al., 2010). Stratigraphic relationships (Loizeau et al., 2012) and cratering ages for the overlying phyllosilicate units give an age for the heavily cratered paleosurface of >4 Gyr. Therefore, this surface cannot be dated directly using cratering ages. The phyllosilicates themselves are dated to $3.8^{+0.2}_{-0.2}$ Ga (Loizeau et al., 2012). The greatest density of well-preserved embedded craters occurs on the underlying paleosurface. Embedded craters in the overlying phyllosilicates are more sparse, perhaps due to dilution of the crater population by sedimentation. During periods of rapid sedimentation, there is less time

Table 1

Image and DTM numbers for Mawrth Vallis and Meridiani Planum crater counting locations

Site	#	Image(s)	DTM
Mawrth	1	ESP_023488_2050/ ESP_023554_2050	DTEEC_023488_2050_023554_2050_A01 (PDS-released)
	2	PSP_008245_2045/ ESP_016394_2045	DTEEC_008245_2045_016394_2045_A01 (PDS-released)
	3	ESP_028011_2055/ ESP_028288_2055	DTEEC_028011_2055_028288_2055_A01 (PDS-released)
Meridiani	4	ESP_022221_1850/ ESP_039667_1850	ESP_022221_1850_ESP_039667_1850_align_1_DEM (email Warren or Kite for copy)

Note. Location numbers (#) correspond to labels shown in Figure 2. Mawrth paleosurface crater counts come from location 1 only. Mawrth phyllosilicate crater counts are a composite of all ancient embedded craters found in visually similar phyllosilicate units in locations 1–3. Meridiani crater counts come from all sedimentary units in location 4 only.

Table 2
Numerical model parameters

Symbol	Units	Description
H	m	scale height
R	$\text{J kg}^{-1} \text{K}^{-1}$	specific gas constant
\bar{T}	K	characteristic atmospheric temperature
g	m s^{-1}	gravitational acceleration
ρ_a	kg m^{-3}	local atmospheric density
ρ_0	kg m^{-3}	surface atmospheric density
z	m	elevation
v	m s^{-1}	speed
t	s	time
C_D	—	drag coefficient
A	m^2	cross sectional area of impactor
m	kg	impactor mass
σ	kg J^{-1}	ablation coefficient
σ_m	MPa	impactor bulk strength
V_t	m^3	transient crater volume
m_f	kg	final impactor mass
v_f	m s^{-1}	final impactor velocity
D_t	m	transient crater diameter
D_f	m	final crater diameter

for craters to accumulate on the same stratigraphic level (Kite et al., 2013). The lower density of craters in the phyllosilicates necessitated crater counting over a larger area. Initially, we compiled crater counts from only images 1 and 2 (Table 1). We later used textural features occurring in aluminum-rich phyllosilicates in HiRISE images 1 and 2 to identify additional outcrops of the same phyllosilicates in nearby regions (i.e., image 3).

2.2. Meridiani Planum

Our study region in Meridiani Planum (Figure 2c, “Meridiani” herein) is located to the southwest of Capen crater. We adopt the crater age of Hynek and di Achille (2017), who date these deposits to $3.82^{+0.10}_{-0.18}$ Ga.

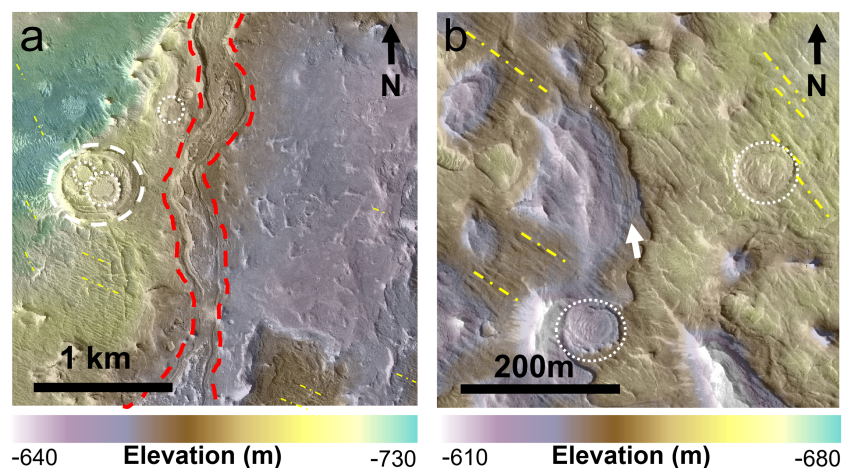


Figure 4. Sedimentary features at Meridiani site (image #4): (a) sinuous ridge (outlined in dashed red, large crater in left of image centered at $12^{\circ}36'45.768''\text{W}$, $4^{\circ}58'11.911''\text{N}$) and (b) layering (white arrow, points at $12^{\circ}36'26.065''\text{W}$, $4^{\circ}46'56.299''\text{N}$). A selection of linear ridges (not interpreted as fluvial) on various stratigraphic levels are marked with yellow dashed-dotted lines. Ancient embedded craters are shown by dashed, white ellipses. Candidate ancient embedded craters (not included in final counts) are marked with a dotted ellipse.

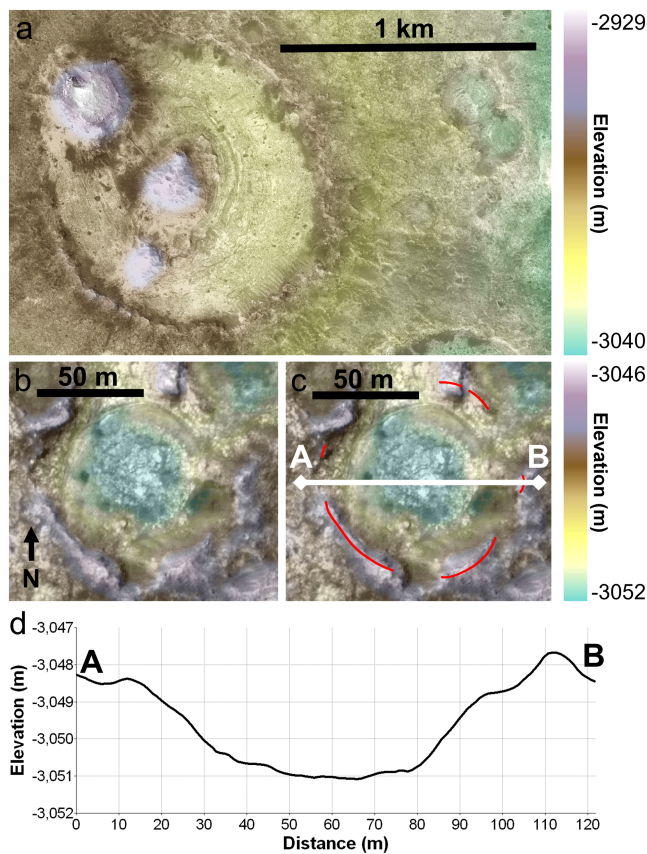


Figure 5. Example ancient embedded craters on Mawrth paleosurface (centered at 21–10' 5.252°W, 24–23' 30.842°N). (a) Large ancient crater, previously identified by Loizeau et al. (2010) (their Figure 8, #2 in Table 1 of this paper), (b) typical, small ancient crater without interpretation, (c) topographically elevated rim outlined in red, (d) cross section showing depth $\ll 0.2 \times$ diameter. #1 in Table 1 and Figure 2. Solar incidence angle 45°. Illuminated by sunlight from NW.

Our DTM includes a sinuous ridge, interpreted as an inverted channel by Davis et al. (2016) (Figure 4a), with some craters embedded in the layered deposits that make up the inverted channel itself. In this study, we are interested in crater populations preserved in sedimentary units. We identify several sedimentary units at our Meridiani site (image #4, Table 1). Light-toned units in the south of the region have horizontal layering (Figure 4b). These light units overlie mid-toned material which has regularly spaced, morphologically consistent ridges with m-scale wavelengths. These have different orientations on different stratigraphic levels (Figure 4b) — this suggests that these are a deposition-era feature re-exposed by more recent differential erosion. We interpret these units as being of sedimentary origin. These units overlie a darker surface with no evidence for a sedimentary origin from HiRISE images. For this study, we only include embedded craters occurring in units with visible sedimentary features and exclude those in areas covered by modern wind-blown material.

3. Method

3.1. Crater Counts

We identify definite ancient embedded craters (Figure 5) according to the following criteria:

1. Approximately circular topographic depression.
2. Topographic feature appears convex-up in anaglyph.
3. $<50\%$ of crater depression obscured by sand/dust infill.
4. Center of the crater sand/dust free.
5. Maximum crater depth $\ll 0.2 \times$ crater diameter.
6. Preservation of a topographically elevated rim spanning at least a 150° arc outside the topographic depression (arc may be discontinuous).

Additional support for a crater being ancient and embedded is the presence of disk-shaped, layered sedimentary deposits inside the crater. However, few embedded craters preserve this feature, and we primarily rely on the criteria listed above. We do not attempt to discriminate between primary and secondary craters in our counts. While secondary craters are

observed on Mars (e.g., McEwen et al., 2005), secondary craters are not observed in Earth's geologic record. We assume that at atmospheric pressures ≥ 1 bar, secondary craters do not significantly affect the observed CSFDs. Additionally, our chosen atmosphere-impactor interaction model (Williams et al., 2014) closely reproduces modern Mars CSFDs without including secondary craters.

We measured ancient embedded craters by placing points along the exposed crater rim in ArcGIS (Figure 5). We fit these points to circles using the MATLAB code `circfit`, generating a best-fit circle as well as the largest and smallest possible circles that fit the measured points. We have attempted to reduce the human errors associated with the crater counts by making at least 2 passes of each DTM. To ensure in-lab consistency, a second person performed an independent crater count within a test region in each DTM. After two independent counts, differences in selections of definite and candidate craters were discussed and were recategorized accordingly. In an 11-km² test patch in DTM #1, Analyst A identified 36 ancient craters, and Analyst B identified 26. Of these, 25 were agreed upon. Eleven craters were identified by Analyst A that were not identified by Analyst B. These craters have a mean diameter 40 m and are all < 75 m in diameter. Due to the small average size of these craters, this difference in identification is likely due to 2 passes of the DTM by Analyst A and only 1 check pass by Analyst B. 1 crater with diameter > 100 m is identified by Analyst B and not by Analyst A. Our fitting procedure is most sensitive to the smallest craters in the population; therefore, the inclusion/exclusion of this crater is unlikely to affect our results. We only use CSFDs with more than ~ 50 craters to reduce the impact of misidentifying erosion-era craters as ancient on the paleopressure fit and to improve our confidence that our measured population more closely represents the erosion-modified ancient crater population (Williams et al., 2017).

3.2. Model

Impactors passing through planetary atmospheres experience ablation and deceleration and can also undergo catastrophic disruption or fragmentation. These processes have been extensively modeled for both the Earth's atmosphere (e.g., Bland & Artemieva, 2006; Boslough & Crawford, 2016; Hills & Goda, 1993; Lyne et al., 1996; Melosh, 1981; Passey & Melosh, 1980; Svetsov et al., 1995) and the atmospheres of other bodies in the Solar System (e.g., Chappelow & Sharpton, 2012; Ivanov, 2001; Popova et al., 2003; Korycansky et al., 2004, 2005). In this study, we employ a numerical model of ablation and deceleration of impactors passing through atmospheres of different pressures written by Williams et al. (2014). This model closely reproduces geologically recent crater populations on Mars when zero-elevation corrected atmospheric pressure is set to the present day value. To estimate paleopressure, we treat impacts as a Poisson process (Aharonson et al., 2003) and use the pipeline of Kite et al. (2014) to Bayesian fit the observed CSFD to model crater distributions at a range of atmospheric pressures from 0.006 to 5 bar, as generated for Kite et al. (2014) using the methodology described in Williams et al. (2014). We briefly summarize the model here. Model parameters are listed in Table 2.

Synthetic crater populations are generated using a forward model of impactor-atmosphere interactions for an ensemble of 10^6 impactors with properties drawn from distributions of size (Brown et al., 2002), velocity (Davis, 1993), density, and strength (i.e., irons and chondrites) (Ceplecha et al., 1998) based on terrestrial fireball network observations (Ceplecha et al., 1998) using a Monte Carlo approach. Each impactor starts at an altitude of 100 km and passes through an atmosphere with scale height:

$$H = \frac{RT}{g} \quad (1)$$

where R is the specific gas constant for CO_2 , and \bar{T} is a characteristic atmosphere temperature. We assume that the atmosphere is isothermal and use surface temperature T_s as our value for \bar{T} . The local atmospheric density, ρ_a is:

$$\rho_a = \rho_0 \exp \frac{-z}{H} \quad (2)$$

where ρ_0 is the surface atmospheric density calculated using the ideal gas law ($p_0 = \rho_0 RT$). p_0 is surface pressure. We assume a flat surface geometry and therefore, do not allow impactors to skip out of the atmosphere (Williams et al., 2014).

As an impactor passes through the atmosphere, it loses kinetic energy through drag (equation (3)) and ablation (equation (4)):

$$\frac{dv}{dt} = -\frac{C_D \rho_a v^2 A}{2m} + g(z) \sin \theta \quad (3)$$

(where t is time, v is speed, z is height above Mars' surface, θ is the angle of the impactor trajectory measured from the horizontal, $g(z)$ is local gravitational acceleration at z , C_D is the drag coefficient, ρ_a is atmospheric density at z , A is cross-sectional area of the impactor). The impactor is assumed to be spherical and in the high Reynolds number, continuum flow regime, therefore $C_D \sim 1$ (Podolak et al., 1988).

$$\frac{dm}{dt} = -\frac{C_h \rho_a v^3 A}{2\zeta} \quad (4)$$

(where m is mass, C_h is heat transfer coefficient, and ζ is the heat of ablation; Williams et al., 2014). C_D , C_h , and ζ are related through the ablation coefficient σ (Ceplecha et al., 1998):

$$\sigma = \frac{C_h}{2\zeta C_D} \quad (5)$$

In addition to ablation, the model includes fragmentation of impactors through aerodynamic breakup. Fragmentation occurs when the dynamic pressure from the impactor passing through the atmosphere ($\rho_a v^2$) exceeds the bulk strength of the impactor (σ_m). All impactors are assumed to have the same bulk strength. $\sigma_m = 0.65$ MPa best reproduces the present-day SFD of small craters on Mars (Williams et al., 2014). The model limits fragmentation to a single event producing < 100 individual fragments, each of which are followed to the end of their flight. As described in Williams et al. (2014), the number of fragments generated in each fragmentation event follows a power-law probability distribution with slope -1.5 . Fragment masses are determined by iteratively subtracting random mass fractions from the initial impactor mass.

Table 3

Impact crater scaling parameters

Parameter	Dry soil/soft rock	Wet soil/hard rock	Description
ρ_t (kg m ⁻³)	2000	3200	Target density
μ	0.41	0.55	Empirical constant related to target porosity (equation (6))
Y (kPa)	65	6900	Yield strength
K_1	0.132	0.095	Empirically-derived scaling parameter (equation (6))
K_2	0.26	0.257	Empirically-derived scaling parameter (equation (6))
K_r	1.1	1.1	Empirically-derived scaling parameter (equation (3.2))

Note. Values as given in Williams et al. (2014) from material published online (<http://keith.aa.washington.edu/craterdata/scaling/theory.png>).

When an impactor reaches the surface, final mass and velocity can be used to calculate the size of the resulting crater (Holsapple, 1993):

$$V_t = K_1 \frac{m_f}{\rho_t} [\pi_2 \frac{\rho_m}{\rho_t}^{\frac{1}{3}} + K_2 \pi_3^{\frac{2+\mu}{2}}]^{-\frac{3\mu}{2+\mu}} \quad (6)$$

where V_t is transient crater volume, m_f is final mass, ρ_t is target density, ρ_m is impactor density, and K_1 , K_2 and μ are empirical coefficients that vary between target material (Table 3). This expression for V_t smoothly spans the transition between the strength regime (crater size primarily determined by target strength) and the gravity regime (crater size primarily determined by surface gravity) (Holsapple, 1993). π_2 and π_3 are dimensionless numbers given by:

$$\pi_2 = \frac{gR_p}{v_f^2} \quad (7)$$

$$\pi_3 = \frac{Y}{\rho_t v_f^2} \quad (8)$$

where v_f is final velocity, R_p is projectile diameter, and Y is target yield strength. Impactors with $v_f < 500$ m s⁻¹ are removed from the simulation because they are travelling too slowly to produce hypervelocity impact craters (Kite et al., 2014; Williams et al., 2014). Transient crater diameter, D_t is then:

$$D_t = 2K_r V_t^{\frac{1}{3}} \quad (9)$$

The final diameter of the crater $D_f = 1.3D_t$ (Holsapple, 1993). When crater clusters form after fragmentation events, their effective diameters (D_{eff}) are calculated from individual crater diameters (D_i) using $D_{eff} = (\sum_i D_i^3)^{\frac{1}{3}}$. The synthetic CSFD assumes target properties for dry soil (Williams et al., 2014). We follow Kite et al. (2014) and assume that target properties for dry soil/soft rock (Table 3) are likely to be appropriate for ancient craters preserved in the Mawrth phyllosilicates and at our Meridiani Planum site because the craters formed during the deposition of loose material. However, the cratering model may be strongly sensitive to target strength (Figure S4 in Kite et al., 2014). The lithology of the Mawrth "dark paleosurface" is poorly constrained (Loizeau et al., 2012), and therefore, values for hard rock may be more appropriate. Additionally, if the sediments deposited at Mawrth Vallis and Meridiani Planum were wet, their strength would be greater (Table 3). Both of these would introduce a systematic underestimate of atmospheric pressure. An increase in target yield strength from dry alluvium ($Y = 65 \times 10^3$ Pa) to hard rock ($Y = 7 \times 10^6$ Pa) without changing any other parameters could increase our upper limit paleopressure estimates by as much as a factor of 2. This only holds if μ (an experimentally derived empirical coefficient related to porosity) is kept constant at $\mu = 0.41$. However, a more appropriate value for μ for hard rock may be $\mu = 0.55$. With this Y -dependent adjustment for the value of μ , our paleopressure estimates would only increase by a factor of $\sim 25\%$ for a hard rock surface.

Our final paleopressure estimates are corrected for elevation to zero-elevation atmospheric pressure:

$$P_{corr} = \frac{P}{\exp \frac{-|\Delta z|}{H}} \quad (10)$$

Table 4*Crater diameters and paleopressure upper limits from models and full fitting procedure*

Site	Min. crater diameter	Paleopressure upper limits	
	D_{\min} (m)	p_{sfd}^N (bar)	p_{sfd}^F (bar)
Mawrth paleosurface	$21.2^{+0.6}_{-0.7}$	1.9 ± 0.1	1.3 ± 0.1
Mawrth phyllosilicates	$15.2^{+0.7}_{-0.9}$	1.5 ± 0.1	1.0 ± 0.1
Meridiani	$15.7^{+1.2}_{-2.0}$	1.5 ± 0.1	1.0 ± 0.1

Note. D_{\min} - minimum measured crater diameter, error bars give upper and lower limits from `circfit` pressure estimates from the full CSFD with (p_{sfd}^F) and without (p_{sfd}^N) fractal correction for each study region. All pressures are zero-elevation corrected.

where p_{corr} is the new elevation corrected atmospheric pressure and $|\Delta z|$ is the change in elevation of the site. Assuming $H = 10.7$ km, this corresponds to a systematic error of $\sim 10\%$ for every 1 km change in elevation. At present, our crater counting sites are 3,100 m (Mawrth) and 670 m (Meridiani) below the Mars geoid. Large (km-scale) changes in the elevation of these sites are not expected between the time of crater population accumulation and present, even taking into account the growth of Tharsis and true polar wander (e.g., Citron et al., 2018).

4. Results

Our paleopressure estimates are 1.9 ± 0.1 bar for the Mawrth paleosurface, 1.5 ± 0.1 bar for the Mawrth phyllosilicates, and 1.5 ± 0.1 bar for the Meridiani data (Table 4). The fitted synthetic CSFDs are shown alongside the real data in Figure 6. Our new upper limits on continuous atmospheric pressure are shown alongside existing paleopressure estimates in Figure 7. Our impactor-atmosphere interaction model produces synthetic CSFDs with 10–20-m diameter craters under a 1 bar atmosphere. This is consistent with observations of small (<100-m diameter), hypervelocity craters on Earth (e.g., Folco et al., 2011; Shoemaker et al., 2005),

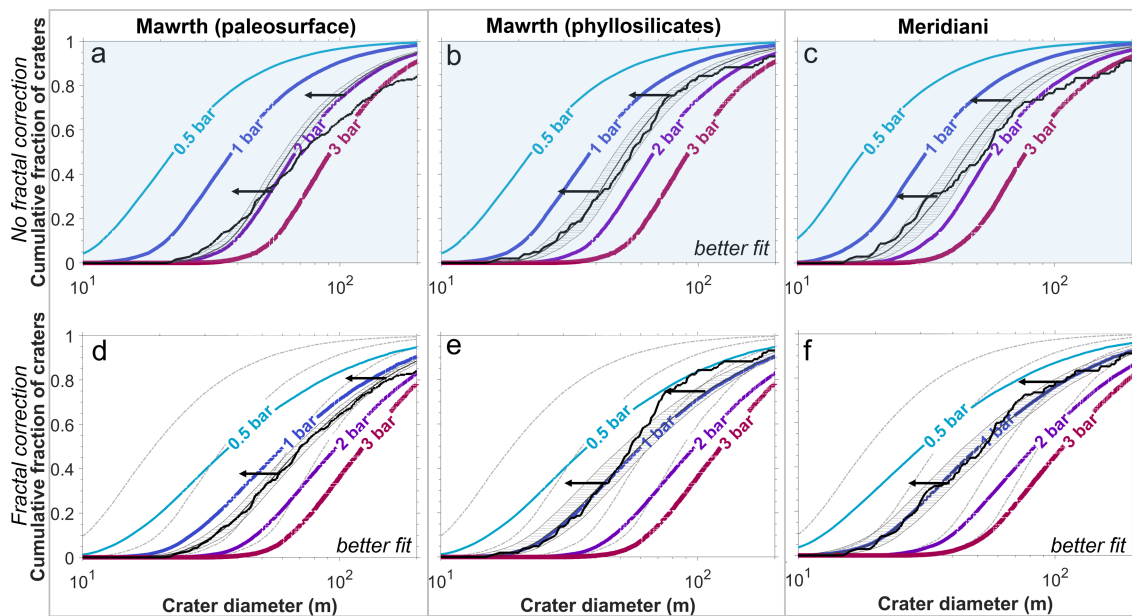


Figure 6. Fits of measured crater size frequency distributions (CSFDs, black) to synthetic data from atmosphere-impactor interaction model (colored lines) without the fractal correction (described in section 5.1, a–c, blue tint) and with the fractal correction (d–f, see discussion in section 5.1) for the Mawrth paleosurface (a, d), Mawrth phyllosilicates (b, e), and Meridiani (c, f). x-axis upper limit is 200 m because fitting procedure is most sensitive to smallest craters in distribution (15–50-m scale). Dashed-dotted, gray lines in d–f show synthetic CSFDs without the fractal correction (from left to right: 0.5, 1, 2, and 3 bars). Hatched areas show 2- σ bootstrap error envelope on fit (± 0.1 bar). Black horizontal arrows indicate that paleopressure fits are upper bounds, due to the possibility of preferential obliteration/non-recognition of small craters, (section 5.3).

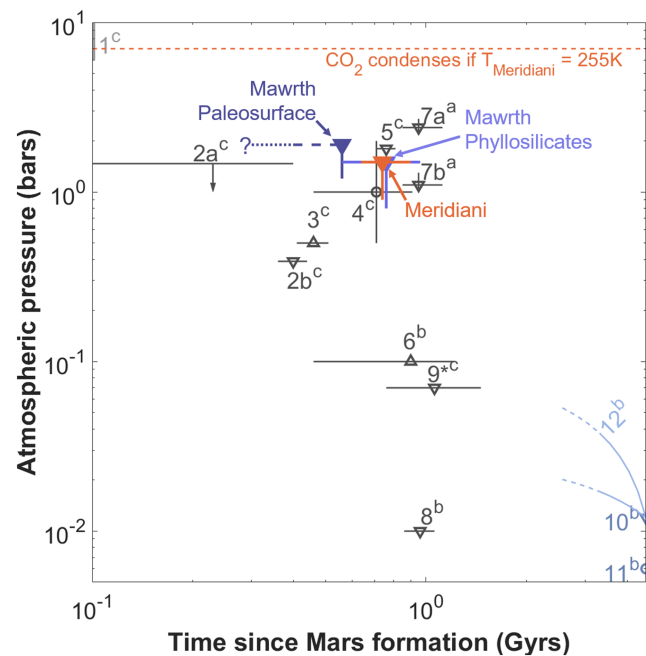


Figure 7. Updated paleopressure constraints for Mars showing our new upper limits (orange, light purple, and dark purple symbols) in context. Superscripts: a - constraints from small, ancient, embedded craters, b - constraints from remote sensing, c - constraints from all other techniques (meteorite analyses and modeling). Upward (downward)-pointing triangles indicate lower (upper) bounds. Circles indicate estimates of absolute atmospheric pressure or direct measurements. Downward arrows from a horizontal line indicate that pressure is constrained to have been below the given value for the *entire* time interval. 1^c) Cosmochemical estimate based on scaling Earth's C abundance to Mars (Lammer et al., 2013), 2^c) atmospheric evolution model results based on Ar isotope measurements from Mars meteorite ALH 84001 and from modern Mars (Cassata et al., 2012) (a - maximum atmospheric pressure for first 400 Myr of Mars' history, b - pressure at age of meteorite), 3^c) atmospheric evolution model results based on Ne, Ar and Xe isotope measurements from ALH 84001 and modern Mars (Kurokawa et al., 2018), 4^c) thermodynamic modeling of Mg-Fe-Ca carbonate formation (van Berk et al., 2012), 5) atmospheric evolution model results (Hu et al., 2015), 6^b) pressure calculated from impact structure from bomb sag in pyroclastic deposits (Manga et al., 2012), 7) pressure estimates from CSFDs in Aeolis Dorsa (corrected from Kite et al., 2014) (a/b - with/without rimmed circular mesas), 8^b) pressure calculated from wind ripple size (Lapotre et al., 2016), 9^c) thermodynamic modeling of siderite formation (Bristow et al., 2017) (since superseded by experimental results, see Tosca et al., 2018), 10^b) annual mean modern atmospheric pressure + CO₂ stored in polar ice (Bierson et al., 2016; Putzig et al., 1987), 11^b) annual mean modern atmospheric pressure, 12^b) absolute upper and lower bounds of MAVEN escape rates extrapolated backwards in time (Lillis et al., 2015). Only studies that explicitly find paleopressure estimates are included here.

including two that are <20-m in diameter within the past 5 kyrs: the Haviland crater (15 m, Nininger & Figgins, 1933), and the Carancas crater (13.5 m, Tancredi et al., 2009).

Using the same method as described here, Kite et al. (2014) stated a paleopressure upper limits of 0.9 ± 0.1 bar and $p < 1.9 \pm 0.2$ bar with and without rimmed circular mesas (potential but not confirmed preserved ancient impact craters), respectively. To do this, the senior author (E. S. Kite) used the p_0 (zero-elevation corrected atmospheric pressure) from the National Space Science Data Center (0.20 kg m^{-3}). However, this greater than the p_0 given by the Mars Climate Database and is not self-consistent. With self-consistent p_0 , the limits become $p < 1.1 \pm_{0.1}^{0.2}$ and $p < 2.4 \pm 0.2$ bar. We plot the corrected values (7b^a and 7a^a) in Figure 7 onwards. Our paleopressure estimates at 3.8 ± 0.2 Ga agree with the constraint of van Berk et al. (2012) (4^c) from thermodynamic models of carbonate cation compositions, and the modeled upper bound on pCO₂ from Hu et al. (2015) (5^c). Including a fractal correction (described in Section 5.1) lowers our paleopressure estimates; we discuss whether the fractal correction is appropriate in Section 5.1. We assume that local, elevation-independent variations in pressure are negligible (we justify this assumption in Section 5.3) and consider the impact of both long-term (10^8 -year timescale) and short-term (on the timescale of obliquity changes) changes in atmospheric pressure on our upper bounds in Section 5.2.

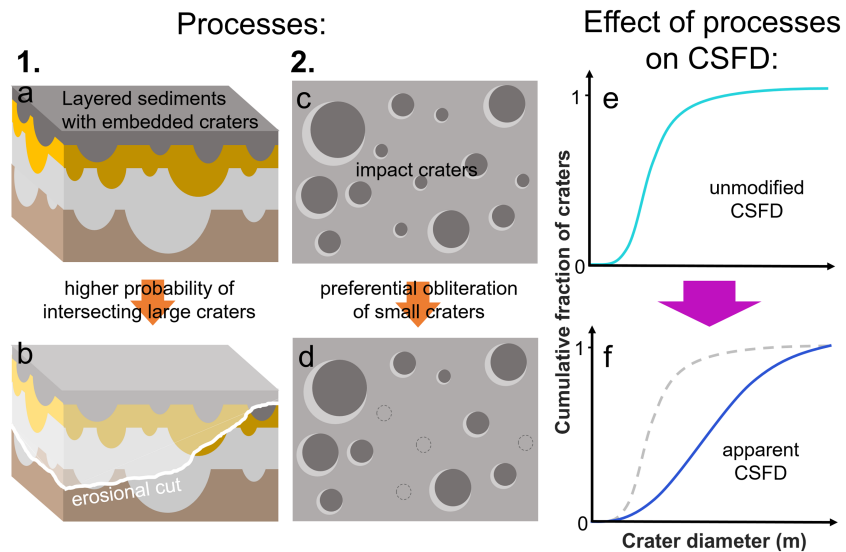


Figure 8. Schematic illustrating the effect that depositional and erosional processes have on CSFD shape. Process 1: (a) initial cratered volume before modification, (b) intersection of erosional cut with cratered volume, cut intersects more large craters than are represented by the underlying crater population. We refer to the correction for this effect as the “fractal correction.” Process 2: (c) initial cratered surface, (d) cratered surface after modification by sedimentary processes with obliterated smaller craters indicated by dashed circles. Effect of these two processes on CSFD: (e) initial CSFD for a & c (pre-modification), (f) observed CSFD for b & d after modification by processes 1 & 2. The grey dashed curve is the original, unmodified CSFD from e.

5. Discussion

Our main points in this section are as follows:

1. Section 5.1 — CSFDs can be modified by multiple processes including changes in impactor population and preferential obliteration of smaller craters. This supports the interpretation of our paleopressure fits as upper limits on atmospheric pressure, rather than best estimates.
2. Section 5.2 — Our measured CSFDs cannot be produced through atmospheric pressures persistently above our upper limits. However, our measured CSFDs *can* be matched by crater population accumulation in either an atmosphere with constant pressure or in an atmosphere that has varied in time between high and low atmospheric pressures. Therefore, our paleopressure estimates from section 4 cannot simply be taken as fixed upper bounds on atmospheric pressure. We can constrain the minimum accumulation time at any pressure < 1.5 bar recorded by each outcrop by using crater production functions.
3. Section 5.3 — Our results are not affected by local variations in zero-elevation corrected pressure, as the early Martian atmosphere is unlikely to have been able to sustain annual mean zero-elevation corrected atmospheric pressure gradients greater than a few percent.

5.1. Modification of CSFDs Over Geologic Time: Sedimentation, Erosion, and Changes in Impactor Population

There are three key processes that contribute to the removal of smaller craters:

1. The likelihood of intersecting a crater on an erosion surface through a 3D volume containing craters is proportional to a crater diameter (Smith et al., 2008, Figures 8a and 8b).
2. Erosion and sedimentation processes preferentially remove small craters because of their smaller topographic expression (Jerolmack & Sadler, 2007; Öpik, 1966), Figures 8c and 8d) (a more complete summary of the issues associated with crater modification and preservation can be found in Williams et al., 2017).
3. Craters may be excluded from counts because the resolution of HiRISE images, and DTMs are insufficient for us to resolve the smallest preserved craters.

These effects increase the likelihood that the smallest craters in any population will be missed in crater counts. As a result, paleopressure estimates based on our measured CSFDs represent upper bounds. Additionally, degradation of craters can widen the apparent crater diameter by up to 10% through backwasting of the crater rim (Craddock et al., 1997; Grant & Schultz, 1993). Watters et al. (2015) also report rim span

widening with increasing crater modification for small, recent craters, that may be in a more representative size regime for the craters that most strongly affect our paleopressure estimates (<100-m diameter). The effect of this is to shift the entire CSFD to larger crater diameters (i.e., displacing the schematic CSFD in Figure 8e to the right), which may mean that our upper bounds on paleopressure are conservative. It is also possible for an erosional cut to occur below the original crater rim. This would lead to apparent shrinkage of the bowl. However, our ancient embedded crater criteria (section 3) specify that a topographically elevated rim *must* be preserved for a crater to be included in our counts, and therefore, this effect is unlikely to be important for our crater counts. We assume that a preserved topographic rim represents the original crater diameter regardless of the orientation of an erosional cut. If the cut destroys the rim — modifying the apparent crater diameter — the crater does not meet the selection criteria and is not included in this study.

To correct for the increased probability of not intersecting smaller craters in an erosional cut that spans many stratigraphic levels (1), we can compensate for the preferential loss of the smallest craters in each population. This can be done by implementing a “fractal correction” (Kite et al., 2014). This fractal correction reduces the weight of each crater in our modelled CSFDs in proportion to its diameter, with the greatest down-weighting of the largest craters, so that each diameter range is an equally good probe of the underlying CSFD throughout the cratered volume that we are only seeing a small part of. To ensure that our paleopressure upper limits are as conservative (high) as possible, we choose not to apply this correction by default. The Mawrth paleosurface data is fit much better by the model data with the fractal correction (accounting for processes 1 & 2) included (Figures 6a–6d). However, the paleosurface dips only 1–2° to the north east, and the erosion surface does not visibly cut any stratigraphic layers. Therefore, we propose that the Mawrth paleosurface represents a single stratigraphic level that has been exposed at the surface by the erosional cut. If this is the case, the fractal correction does not apply.

While we do not rule out the possibility of size-selective crater obliteration (2) as an explanation for this observation on the Mawrth paleosurface, a fourth process may contribute to the difference in observed CSFD:

4. The impactor population in our atmosphere-impactor interaction model might not be representative of the impactor flux at Mars' orbit at ~4 Ga (Strom et al., 2005).

The impactor population used in the forward model is adapted from satellite observations of the annual flux of objects colliding with Earth. This is scaled to Mars and can closely reproduce recent crater populations on Mars (Williams et al., 2014). However, it may not be a representative of Mars' impactor population over the past 4 Gyr. The Mawrth paleosurface CSFD may record a difference in the impactor population reaching Mars earlier in its history, as a reduction in the relative proportion of smaller impactors for a given atmospheric pressure would have the same sign as the fractal correction, acting to flatten the cumulative CSFD. Additionally, the Mawrth phyllosilicates and Meridiani CSFDs may also encode a changing impactor population component, as their ages place them close to the end of the Late Heavy Bombardment, for which evidence suggests an impactor CSFD richer in massive impactors by 1 log unit (Strom et al., 2005, 2015).

The Meridiani data are also better fit when the fractal correction is implemented (Figures 6c vs. 6f). This is consistent with the fact that the Meridiani crater counts are a composite of ancient embedded craters in sedimentary deposits that span multiple stratigraphic levels, few of which are as exposed at the surface over as large a continuous area as the Mawrth paleosurface. However, the Hynes and di Achille (2017) age for this region also places it towards the end of the Late Heavy Bombardment. Therefore, a change in impactor population (4) may partially explain the shape of the CSFD by increasing the proportion of large impactors, flattening the CSFD. Conversely, the Mawrth phyllosilicate data are fit best by the model CSFDs when no fractal correction is applied (Figures 6b vs. 6e). This is surprising because, like Meridiani, the Mawrth phyllosilicates crater counts also span multiple stratigraphic levels, which we would expect to flatten the observed CSFD due to the greater probability of an erosional cut intersecting larger craters (1). The difference in the two CSFDs may reflect differences in crater preservation between the two sites. Alternatively, the dominant effect may be changes in impactor population between the deposition of the Mawrth phyllosilicates and Meridiani sediments, as the Mawrth phyllosilicates could predate the Meridiani deposits by up to ~300 Myr based on cratering ages.

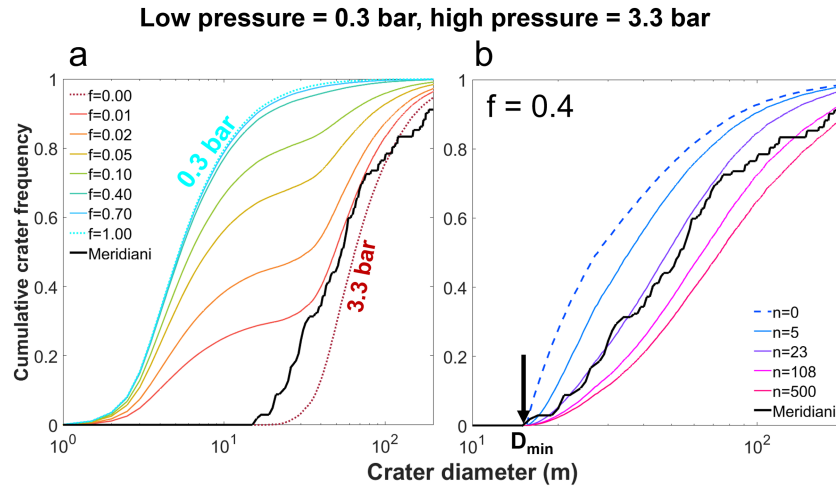


Figure 9. Model crater size frequency distributions (CSFDs) produced by (a) variations in atmospheric pressure from 0.3 to 3.5 during the time of crater population accumulation (b) degree of preferential obliteration of small craters. Dashed colored lines correspond to nonvarying 0.3 (cyan) and 3.5 bar (red) atmospheres. f is the fraction of time spent at minimum atmospheric pressure. Thick black line shows measured Meridiani CSFD. To illustrate the effect of simulated crater population modification on synthetic CSFDs, (b) shows a time-varying pressure CSFD with $f=0.4$ and different degrees of preferential obliteration of small craters (n).

5.2. Constant and Time-Varying Atmospheric Pressure Both Fit Data

Crater *populations* do not record an instantaneous atmospheric pressure, and atmospheric pressure need not remain constant over time. Long-term changes in the balance between atmospheric source and sink processes may have changed atmospheric pressure over the course of crater accumulation. The large number of craters on the Mawrth paleosurface suggests that it was exposed for >100 Myr (Loizeau et al., 2010). This is not much shorter than the timescales of degassing, weathering, and atmospheric escape for early Mars. Additionally, climate models have demonstrated that, depending on Mars' obliquity history, its atmosphere may have undergone periods of collapse (e.g., Forget et al., 2013; Kreslavsky & Head, 2005; Saito & Kuramoto, 2017; Soto et al., 2015) and reinflation. This provides a mechanism for atmospheric pressure to vary on 10^3 yr timescales, provided that the atmospheric pressure falls below the threshold pressure for atmospheric collapse (~ 0.5 bar according to Forget et al., 2013). If either of these processes occurred, then our measured CSFDs may represent time-varying atmospheric pressures.

We used synthetic crater populations generated by the atmospheric filtering model to create 'time-varying pressure' CSFDs (S_{mix}). We achieve this by combining CSFDs for a chosen maximum and minimum pressure. These are weighted by the fraction f of time spent at the minimum pressure. CSFDs at high and low pressures are normalized so that the number of large impactors reaching the surface after passing through either atmosphere are the same. We test combinations of 0.007, 0.3, 0.5, 1.2, 2.3, and 3.5 bar atmospheres. No fractal correction is applied to these CSFDs.

$$S_{mix} = fS_{low} + (1 - f)S_{high} \quad (11)$$

When the atmosphere is thin, a greater number of small impactors are able to reach the surface over any given time period. Spending as little as 0.1% of the crater accumulation period at the lower pressure can form a substantial "tail" of small craters (Figure 9a). However, we may not actually be able to resolve the small crater tail in our data because of observational limitations (the resolution of HiRISE images and DTMs), and because the crater population has been modified by sedimentation and erosion.

We approximate the effects of sedimentation and erosion on a given CSFD (S) by multiplying through by an arbitrary crater removal factor (c), which is a function of crater diameter such that:

$$c = \begin{cases} 0, & D < D_{min} \\ 1 - \exp\left(-\frac{D_{min}-D}{n}\right), & D \geq D_{min} \end{cases} \quad (12)$$

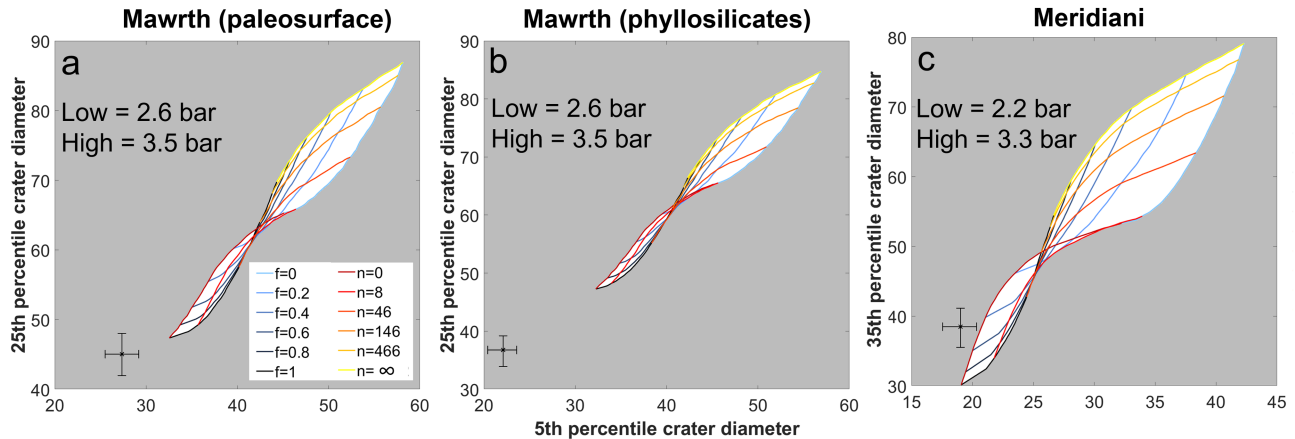


Figure 10. Our measured crater size frequency distributions (CSFDs) cannot be produced by any combination of atmospheric pressures above our continuous paleopressure upper limits, even when the CSFDs are modified by preferential removal of small craters. Contours of 5th and 25th (Mawrth paleosurface and Mawrth phyllosilicates data) and 5th and 35th (Meridiani) crater diameter for different fractions of time spent at low pressure (f , cool colors) and degrees of CSFD modification by preferential obliteration of small craters (n , warm colors) plotted on the same axes as the actual 5th and 25th percentile crater diameters for each site (black crosses with error bars). The 5th and 25th (35th) percentiles correspond to the small craters in the distribution. Error bars indicate mean difference between best-fit crater diameter and maximum and minimum crater diameters found using `circfit`. Greyed out areas are regions of parameter space for which it is not possible to reproduce the shape of the measured CSFD. High and low pressures are corrected to planet datum elevation (i.e., pressures are corrected from local site elevation to 0-m elevation).

We use this to generate a "modified" CSFD, S_{mod} :

$$S_{mod} = c(D)S \quad (13)$$

where D_{min} is the smallest observed crater diameter for a given dataset and n is the "e-folding" crater diameter, such that $\sim 60\%$ of craters with $D = n + D_{min}$ are preserved. This simple approximation of small crater removal is justified based on the possible CSFD modification mechanisms outlined in section 5.2, all of which act to preferentially remove smaller craters. Our approach also gives the worst case scenario for crater preservation because we assume that the smallest *possible* crater in each CSFD is the smallest *observed* crater in our crater counts. We take D_{min} from each CSFD rather than using an overall D_{min} because ancient embedded craters on the Mawrth paleosurface are visually distinct from those preserved in the Mawrth phyllosilicates or Meridiani units. Therefore, we cannot assume that all of the crater populations have been preserved in the same way or have undergone the same modification.

To compare our artificial, cumulative CSFDs for time-varying atmospheric pressure to our measured CSFDs, we plot the 5th and 25th (Mawrth paleosurface and phyllosilicates) and 5th and 35th (Meridiani) percentile crater diameters from the artificial populations and our real data (Figure 10). If our measured crater diameters fall within the range of diameters for each percentile that can be achieved by changing the fraction of time spent at low pressure (f) and changing the degree to which the population is modified by the preferential removal of small craters (n) for a combination of pressures, then our data can be reproduced by having an atmosphere varying between these two pressures during crater accumulation. We demonstrate that it is *not* possible to match the 5th and 25th (35th) percentile crater diameter for any combinations of pressures greater than the upper limit on continuous atmospheric pressure presented in section 4 (Figure 10). This is because the CSFDs for a high pressure atmosphere are more strongly dominated by larger craters, and our population modification function preferentially removes *smaller* craters. This acts to flatten the CSFD and causes high pressure CSFDs to rotate clockwise relative to our data. This generates a greater *apparent* paleopressure. We conclude that our measured CSFDs cannot be produced by atmospheric pressures continuously above our paleopressure upper limits. This is a key finding which validates our main results in Section 4.

However, many different combinations of maximum and minimum pressures can reproduce our observed CSFDs (Figure 11). Therefore, our method cannot rule out changes in atmospheric pressure during crater population accumulation. These changes in atmospheric pressure can occur through:

1. Large scale changes in sources and sinks

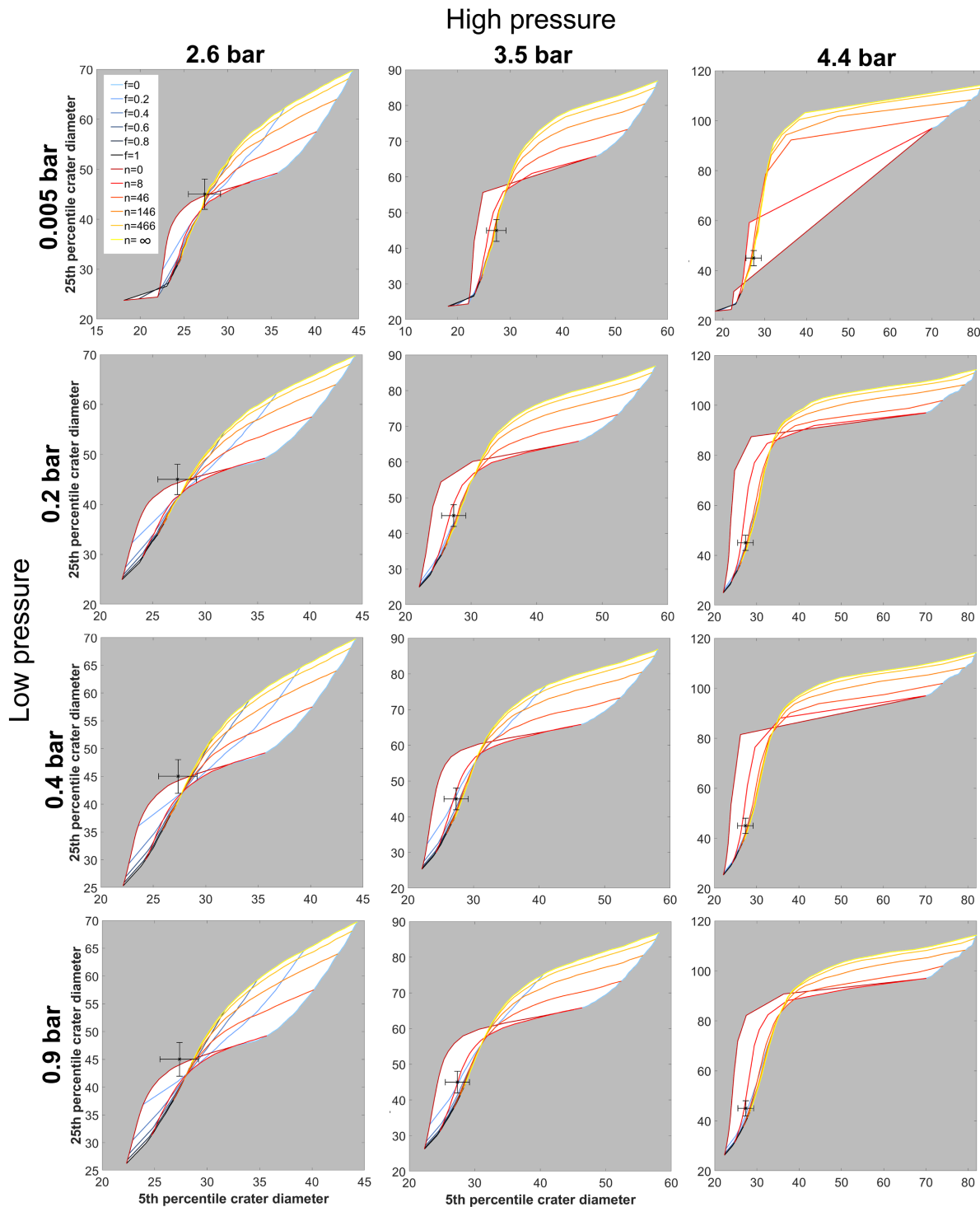


Figure 11. Our measured crater size frequency distributions (CSFDs) can be produced by time varying atmospheric pressure, provided that at least the minimum pressure is below our continuous paleopressure upper limits. Contours of 5th & 25th crater diameter for different fractions (f) of time spent at low pressure (cool colours) and degrees of CSFD modification (n) by preferential removal of small craters (warm colors) plotted on the same axes as the actual 5th and 25th percentile crater diameters for the Mawrth paleosurface (black crosses with error bars). Error bars indicate mean difference between best-fit crater diameter and maximum and minimum crater diameters found using `circonfit`. Greyed out areas are regions of parameter space for which it is *not* possible to reproduce the shape of the measured CSFD. All pressures are corrected to planet datum elevation (i.e., pressures are corrected from local site elevation to 0 m elevation).

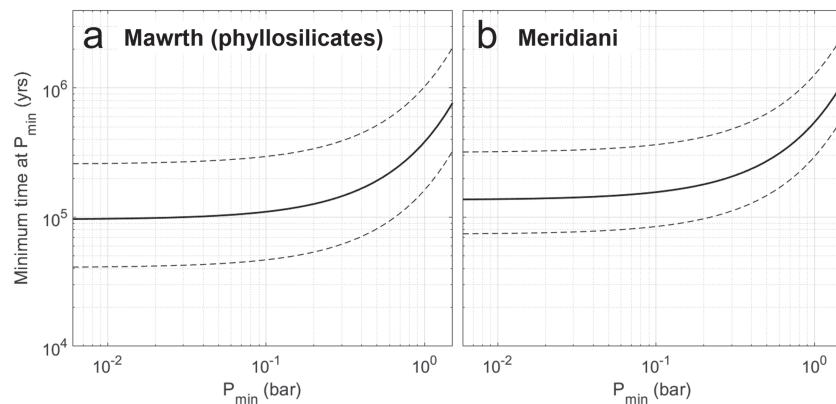


Figure 12. Minimum time needed for the observed number of craters in the diameter bin 15.6–22.1 m to accumulate as a function of minimum atmospheric pressure (P_{\min}) for crater populations (a) in the Mawrth phyllosilicates, (b) at Meridiani. Solid curves show minimum accumulation times at each pressure if both sites are at their best-fit ages (3.8 ± 0.2 and $3.82^{+0.10}_{-0.18}$ Ga, respectively). Dashed curves show minimum accumulation times at each pressure for the upper and lower limits on the ages of each site. X-axis range is 0.006 to 1.5 bar.

2. Atmospheric collapse

Using crater production functions, we can estimate the minimum duration of time spent at present day atmospheric pressure. By selecting a diameter bin in a crater population of a known age, we can estimate the *minimum* accumulation time needed for the number of craters in that bin to accumulate at present-day atmospheric pressure. We observe seventeen 15.6 to 22.1-m diameter craters (bin -1 Michael, 2013) at our Meridiani site. This is the first diameter bin to have > 5 craters. This is important because it means that the crater diameter bin used does not represent the smallest possible crater that *can* form at 1.5 bar (this would yield an infinite accumulation time). Using the production and chronology functions given in Michael (2013), under a paleo-atmospheric pressure of 6 mbar that does not vary during the period of crater accumulation recorded by the embedded craters in our study, our observed crater populations would have accumulated over a minimum of 10^4 years (Mawrth phyllosilicates site) to 10^5 years (Meridiani). At higher atmospheric pressures, fewer craters of this size are expected to form, and a correspondingly longer time must be spent at high pressure to accumulate the observed craters (Figure 12). We can multiply the accumulation time by the ratio of the flux of craters in the chosen diameter bin at present day pressure to the flux of craters in the same bin at a higher pressure. For a paleo-atmospheric pressure of 1.5 bar that does not vary during the period of crater accumulation recorded by the embedded craters in our study, our observed crater populations would have accumulated over a minimum of 10^5 years (Mawrth phyllosilicates site) to 10^6 years (Meridiani site). This calculation cannot be performed for the Mawrth paleosurface because crater production functions do not extend to before 4 Ga. All accumulation time estimates are subject to the uncertainties associated with the dating of the Mawrth phyllosilicates and Meridiani site, as well as uncertainties in the crater production functions used to calculate past cratering rate. If the crater population is older (younger), the flux of craters $\text{km}^{-2} \text{Ga}^{-1}$ is higher (lower) (Michael, 2013), and the observed craters will need a shorter (longer) minimum accumulation time at any given pressure.

We expect smaller craters to be preferentially removed or missed in our crater counts. Therefore we consider it more likely that our measured CSFD for Meridiani corresponds to continuously low ($\ll 1.5$ bar) pressures rather than long periods spent at pressures $\gg 1.5 \pm 0.1$ bars with short (10^4 yr), low pressure excursions. This is further supported by the models of Forget et al. (2013) and Soto et al. (2015), which suggest that there are two different ways that the saturation vapor pressure of CO_2 can affect Mars' atmospheric pressure:

1. Obliquity-independent buffering of high atmospheric pressures to values below the saturation vapor pressure of CO_2 at the coldest point on Mars.
2. Obliquity-dependent collapse into CO_2 icecaps between <0.1 and ~ 0.5 bar.

This suggests that rapid oscillation between pressures >1.5 bar and <0.5 bar is unlikely to be possible through atmospheric collapse because the upper bound on atmospheric pressure for collapse to occur at any obliquity is relatively low (0.5 bar, Forget et al., 2013). Therefore, for any time during crater population accumulation to have been spent at pressures >1.5 bar, 100 Myr-timescale changes in atmospheric pressure due to

processes such as outgassing, impact delivery/erosion of volatiles, carbonate formation, and escape to space must also have occurred. These processes all leave imprints on Mars' geologic record that can potentially be compared to the timing of our measured crater populations to assess the feasibility of different atmospheric pressure histories and are constrained by factors such as the growth of Tharsis (Phillips et al., 2001), shutdown of the Martian geodynamo, and reduction in atmospheric escape rates over time (Tian et al., 2009).

We can therefore identify three very different, pressure histories for Mars between ~ 4 and 3.8 ± 0.2 Ga that are equally consistent with our new results:

1. Pressure continuously *at* our upper limits on continuous atmospheric pressure.
2. Pressure continuously *below* the upper limit for atmospheric collapse (~ 0.5 bar), with possible low pressure intervals caused by collapse.
3. Fluctuations in atmospheric pressure of several bar due to changes in the balance of atmosphere sources and sinks. The minimum atmospheric pressure *must* be below our upper limits on continuous atmospheric pressure.

5.3. Single-Site Atmospheric Pressure Upper Limits are Globally Representative

Having demonstrated that our paleopressure estimates do in fact constrain atmospheric pressure at the time of crater population accumulation, we show that paleopressure at an individual site is representative for all of Mars once corrected for the exponential decrease in local surface pressure with increasing local elevation. On Earth, zero-elevation corrected annual mean pressures vary only by several percent (Trenberth et al., 1987). As our paleopressure estimates are similar to the surface pressure of present day Earth, we expect that pressure gradients in the ancient Martian atmosphere would be of a similar order. However, on some solar system bodies, such as Io, it is possible to sustain gradients in zero-elevation corrected pressures on the order of 10 times mean atmospheric pressure (Buratti et al., 2011; Jessup et al., 2004). Assuming geostrophic balance (latitudinal pressure gradients balanced by Coriolis force) in a 1 bar Martian atmosphere, we can calculate a geostrophic wind velocity, u_g , for a pressure difference of $\Delta p = \frac{1}{5} p_{atm} \sim 2 \times 10^4$ Pa:

$$u_g = \frac{1}{\rho_0 f} \frac{\partial p}{\partial y}, \quad (14)$$

where f is the Coriolis parameter $f = 2\Omega \sin \phi$ (Ω - Mars rotation rate $\sim 7.1 \times 10^{-5} \text{ rad s}^{-1}$, ϕ - latitude ($^\circ$)).

$$p_{atm} = \rho_0 g h. \quad (15)$$

The density of Earth's atmosphere is $\approx 1 \text{ kg m}^{-3}$, and Mars' gravity is approximately three times less of the Earth. Assuming the scale heights to be comparable for both planets, we take $\rho_0 \approx 3 \text{ kg m}^{-3}$ for Early Mars. For $\phi = 30^\circ$, and using the equator-pole distance as a representative length scale $L \sim 5 \times 10^6 \text{ m}$, $u_g \approx 30 \text{ m s}^{-1}$. If the Rossby number $Ro = \frac{U}{fL} \ll 1$, then geostrophic balance is a valid assumption. For $u_g = 20 \text{ m s}^{-1}$ $Ro \approx 0.1$. Assuming that the ideal gas law holds and the difference in pressure is sufficiently small, we can say that:

$$\frac{\Delta T}{T} \propto \frac{\Delta p}{p} \quad (16)$$

This allows us to define a pressure relaxation timescale τ_p :

$$\tau_p \propto \frac{T}{u_g \frac{\Delta T}{\Delta y}} \propto \frac{pL}{u_g \Delta p} \quad (17)$$

This gives $\tau \sim 12$ days.

Maintaining a pressure gradient requires an energy input. Pressure has units of energy density. We can imagine a simple case where energy (Q) is supplied via a region of high surface temperature that heats the overlying CO_2 atmosphere with mass $m = \frac{p}{g}$ initially at $\sim 300 \text{ K}$ to a temperature sufficient to produce the pressure difference of $2 \times 10^4 \text{ Pa}$ (equation (18)). This area needs to supply energy above that supplied to the rest of the atmosphere to maintain the pressure gradient.

$$Q = \frac{p}{g} c_{p_{\text{CO}_2}} T \frac{\Delta p}{p} \quad (18)$$

This energy needs to be supplied on a timescale $\leq \tau$, which tells us the rate at which energy needs to be supplied to the atmosphere to sustain the pressure difference, $\sim 1.3 \times 10^3 \text{ W m}^{-2}$. It is very difficult to devise a mechanism to maintain a rate of energy supply on this scale. From the Stefan-Boltzmann equation, $F = \sigma T^4$, this would require the region of elevated surface temperature to be at around 420 K: 120 K higher than the background. The lower the background surface temperature, the greater this difference would need to be. This surface temperature anomaly would need to span an area comparable to the area of the p anomaly in order to sustain it, otherwise all heat would rapidly dissipate in the surrounding atmosphere. Alternatively, the source of the anomaly would need to be immediately adjacent to one of our study regions. Additionally, for the pressure anomaly to have a significant effect on the observed CSFD, the energy source would need to persist for millions of years. For comparison, typical cooling timescales for magmatic intrusions are on the order of kyrs (Costa et al., 2008). Additionally, lavas could not supply the required power due to the formation of chill crusts (e.g., Matson et al., 2006). Giant impacts have been proposed as a mechanism for raising the surface temperature through the delivery of large amounts of kinetic energy (e.g., Segura et al., 2012). However, modelling studies of impacts on this scale suggest that the heating effect would be 1) global, and 2) short-lived (< 10 years) (Steakley et al., 2019; Turbet, Gillmann, et al., 2019).

We also consider the maximum pressure gradient that could be sustained on Early Mars by differences in insolation across the surface. Assuming an obliquity of 0° , insolation will vary from a maximum at the equator to 0 at the poles. Taking Earth's solar constant to be $G_{SC_{Earth}} = 1361 \text{ W m}^{-2}$ and a Sun at 70% of its current brightness at ~ 4 Ga (Bahcall et al., 2001; Gough, 1981), we can construct an expression for maximum insolation (F_{max}) on Mars:

$$F_{max} = \frac{G_{SC_{Earth}}}{\left(\frac{R_{Earth}}{R_{Mars}}\right)^2} \times \frac{0.7}{\pi} = 131.7 \text{ W m}^{-2} \quad (19)$$

where R_{Earth} and R_{Mars} are distances to each planet from the Sun. Using the pressure relaxation timescale from equation (18) gives $Q = 5.83 \times 10^6 \text{ J m}^{-2}$. Rearranging equation (18) and assuming an average surface temperature of 273 K, the maximum possible zero-elevation corrected pressure difference is only of order 1190 Pa, or $\sim 1.2\%$ of the total atmospheric pressure. Even in the most extreme case where the average Martian surface temperature is low (210 K) and the sun at 4 Ga is assumed to be as bright as at present, this value only rises to 2160 Pa, or less than $2.2\% p_{atm}$. Therefore, we conclude from these order of magnitude estimates that the paleopressure estimates in this study can be taken as representative of the global Martian atmosphere.

6. Integrating New Constraints with Existing Data Using a 2-Component Atmospheric Evolution Model

Detailed atmospheric evolution models rely on balancing fluxes from atmospheric sources and sinks (e.g., Cassata et al., 2012; Dong et al., 2018; Haberle et al., 1994; Jakosky, 2019; Kurokawa et al., 2018; Pepin, 1994; Slipski & Jakosky, 2016). The main sources for the Martian atmosphere are mantle outgassing and impact delivery of volatiles (Jakosky et al., 2018; Sakuraba et al., 2019). There may be additional contributions from retention of a nebular atmosphere (Saito & Kuramoto, 2017) and thermal decomposition of carbonates (Glotch & Rogers, 2013; Pollack et al., 1987). Mantle outgassing throughout Mars' history can be estimated from the rate of crustal production, which has decreased over time, as suggested by geologic evidence (Greeley & Schneid, 1991; Nimmo & Tanaka, 2005; Tanaka et al., 2003), and thermal evolution models (Hauck & Phillips, 2002; Morschhauser et al., 2011). The amount of volatiles outgassed depends strongly on the volatile content of Mars' mantle, which is not well constrained. Phillips et al. (2001) suggest that the growth of Tharsis may have contributed up to 1.5 bar of CO_2 ; however, depending on Martian mantle redox state, outgassed CO_2 may not have been sufficient to make a significant difference to atmospheric pressure (Stanley et al., 2011). The possible major sinks for the atmosphere are escape to space (Chassefière et al., 2007; Dong et al., 2018; Jakosky et al., 2018), impact erosion of the atmosphere (Pham & Karatekin, 2016; Schlichting et al., 2015), carbonate formation (Stephens & Stevenson, 1990; Wray et al., 2016), surface weathering (Baker, 2017), transport of CO_2 into the subsurface (Kurahashi-Nakamura & Tajika, 2006; Manning et al., 2019), and condensation into ice caps (Bierson et al., 2016). Ion escape, sputtering, and photochemical loss mechanisms such as dissociative recombination are all strongly dependent on solar EUV flux and solar wind mass flux (e.g., Ayres, 1997; Brain et al., 2016; Chassefière & Leblanc, 2004) which have

both decreased over geologic time (e.g., Dorren & Guinan, 1994; Tu et al., 2015). However, many of these processes are poorly constrained. We therefore chose to construct a basic, 2-component, process-agnostic model that gathers all sources and all sinks into one term each. The purpose of this exercise is to explore the most simple possible pressure evolution tracks for Mars' atmosphere that satisfy existing paleopressure constraints.

In our model, we express sources and sinks as either a power-law of the form:

$$\frac{dp}{dt}_{(source,sink)} = k_{(1,3)} t^{-k_{(2,4)}} \quad (20)$$

or an exponential:

$$\frac{dp}{dt}_{(source,sink)} = k_{(1,3)} \exp \frac{-t}{-k_{(2,4)}} \quad (21)$$

where k_1 , k_2 (sinks), k_3 and k_4 (sources) are free parameters. For the case shown in Figure 14 (10,000 combinations of k_{1-4}), we select 10 uniformly spaced values of k_{1-2} between maximum and minimum values tuned to span the range that gives the greatest density of solutions in pairs plots for each source-sink set-up. For k_{3-4} , 10 uniformly logarithmically spaced values are selected between maxima and minima found in the same way. This gives four possible source-sink set-ups (1. exponential source + exponential sink, 2. powerlaw source + exponential sink, 3. exponential source + powerlaw sink, and 4. powerlaw source + powerlaw sink). From our tuning process, k_{1-4} are always positive. This is appropriate because we expect both sources and sinks to diminish forward in time (e.g., Jakosky & Phillips, 2001). Overall change in atmospheric pressure at each timestep is given by:

$$\frac{dp}{dt}_{(net)} = -\frac{dp}{dt}_{(sink)} + \frac{dp}{dt}_{(source)} \quad (22)$$

To find k_{1-4} , we use the upper limits of existing paleopressure estimates as hard constraints (shown in Figure 7), and implement the constraint that $\frac{dp}{dt}$ at $t = 0$ must be less than the maximum observed MAVEN loss rate (12^b). We exclude the cosmochemical estimate for Mars' initial CO₂ inventory (1^c) because this value is an estimate and an unknown proportion of the initial volatiles may remain in the mantle. We exclude the constraint given by Kurokawa et al. (2018) (3^c). Their models conclude that the atmosphere must have been uncollapsed at 4.1 Ga to reproduce observed noble gas isotopic compositions in ALH84001 and the modern Martian atmosphere. In their models, the collapse threshold is fixed at 0.5 bar. However, the collapse threshold varies depending on obliquity (Forget et al., 2013; Soto et al., 2015; Nakamura & Tajika, 2003). Mars' obliquity history is chaotic and poorly constrained (Laskar et al., 2004; Touma & Wisdom, 1993), and therefore, the Kurokawa et al. (2018) lower limit may in fact be several times lower. Finally, we exclude the paleopressure estimate of Bristow et al. (2017) (9^{*c}), which was based on reaction-transport modeling of siderite stability. Their models have been superseded by more recent experimental results of Tosca et al. (2018). Tosca et al. (2018) demonstrate that siderite can in fact form at higher pCO₂ under expected early Mars conditions.

We integrate equation (22) backwards in time, starting at a present day atmospheric pressure of $p_0 = 0.012$ bar (i.e., including CO₂ stored in ice caps) with the maximum atmospheric loss rate constrained by the upper limit of the observed MAVEN loss rates (Lillis et al., 2015). This means that we do not prescribe an initial atmospheric pressure for Mars. However, we do force $p > 0$ bar at 4.16 Ga, as this is the age of the earliest paleopressure constraint from the isotopic composition of ALH84001 (Cassata et al., 2012), so we assume that some atmosphere must have been present at this time in order for an "atmospheric component" to be trapped in the meteorite. Our model does not allow negative atmospheric pressures. If pressure becomes negative at any timestep it is reset to 0 bar.

The four possible exponential powerlaw combinations for sources and sinks generate a wide variety of possible pressure histories for Mars. We treat each of the four combination as equally likely. While we do not seek to accurately reproduce Mars' atmospheric pressure history, these models give a qualitative impression of pressure histories allowed by the current data. Therefore, due to the lack of constraints after 3.6 Ga — with the exception of measured MAVEN loss rates — we limit our discussion to atmospheric pressure between 4.3 and 3.6 Ga.

As expected, our model is most strongly affected by the lowest implemented paleopressure constraint. However, a common feature of our initial paleopressure tracks is a low initial atmospheric pressure, typically < 0.5 bar (Figure 14). This agrees with constraints from modeling of noble gas isotope evolution from ALH84001 to present (Cassata et al., 2012), which suggest that atmospheric pressure was < 1.5 bar for the first 400 Myr of Mars' history. However, it does not agree with the thick atmospheres invoked in current models of greenhouse warming of early Mars to ~ 273 K (e.g., Turbet, Tran, et al., 2019; Ramirez, 2017; Wordsworth et al., 2013). Although there is no region of parameter space for which our set-up can include both the Home Plate bomb sag constraint (Manga et al., 2012, 6^b) and wind ripple constraints (Lapotre et al., 2016, 8^b), it is possible to imagine a pressure history involving rapid changes in atmospheric pressure to satisfy both constraints at their published ages (Figure 15). If the wind ripple estimate (Lapotre et al., 2016, 8^b) is implemented as a constraint, the only other paleopressure estimate that affects the permitted solutions is from the Cassata et al. (2012) result ($2b^c$) (Figure 4b). This set-up also gives rise to many solutions in which atmospheric pressure $<$ present for much of Mars' history. In the case where the Home Plate bomb sag constraint (Manga et al. (2012), 6^b) is implemented, the Cassata et al. (2012) result ($2b^c$) is the dominant control on the permitted paleopressure histories. This is most likely because this is the earliest constraint and therefore sets the effective maximum pressure because the majority of values for k_{1-4} generate pressure histories that decrease towards the present (we do not implement episodes of atmospheric collapse in our maximally simple model). As discussed in section 4, applying a fractal correction to our synthetic CSFDs lowers our paleopressure estimates. However, when Cassata et al. (2012) ($2b^c$) is implemented as a constraint, pressure is already too low by 4 Ga for our new estimates to impact the allowed paleopressure histories, regardless of whether Manga et al. (2012) (6^b) or Lapotre et al. (2016) (8^b) are implemented as constraints. This emphasizes the impact of early paleopressure estimates on our understanding of Mars' atmospheric evolution over time. This is inconsistent with geologic evidence for surface liquid water on Mars, as present day annual mean temperatures and pressures do not allow for channel-forming quantities of liquid water to be stable on Mars' surface even at higher solar luminosities. It is currently unclear whether the existing rock record on Mars extends before 4 Ga; therefore, it is not possible to apply the technique used in this paper to this time period, if indeed the interpretable-from-orbit Martian sedimentary rock record extends back this far.

Figure 14c shows the permitted pressure histories if only paleopressure upper limits from small exhumed crater methods (i.e., this paper and Kite et al., 2014) are enforced as constraints. The narrow time window covered by our new upper limits means that the majority of Mars' atmospheric evolution is poorly constrained by these data, and a much wider range of paleopressure histories are permitted. This gives rise to two separate regions of maximum solution density in time-pressure space. The first cluster of solutions starts between 0.5 and 1.8 bar early in Mars history and remains steady ~ 4 Ga when pressure begins to decrease towards present day values. The second cluster starts at ~ 0.012 bar (i.e., modern atmospheric pressure if ice caps are included (Bierson et al., 2016) and remains at approximately constant pressure for all of Mars history. There is also a third cluster with a lower density of solutions that start off at very high initial atmospheric pressure (of order 10s of bars). This exceeds the cosmochemical estimate of Mars' initial volatile inventory (Lammer et al., 2013), but these pressure histories cannot be ruled out by CSFD-based paleopressure estimates alone due to the absence of cratering ages before 4 Ga and because Mars' sedimentary record may not extend this far back in time.

The lack of paleopressure estimates prior to 4 Ga and after 3.6 Ga makes it difficult to meaningfully assess the sensitivity of our model to each individual constraint. Once again, this motivates a search for more paleopressure constraints both between 3.6 Ga and present, and deep in Mars' history. Our CSFD method can only be applied where craters are embedded in stratigraphy. While we have focused on using orbiter data to investigate sedimentary rocks that may preserve evidence for liquid water on or near the Martian surface during deposition (Malin & Edgett, 2000), it may be possible to apply the technique to aeolian sediments in the search for more recent paleopressure estimates (e.g., Nuno & Paige, 2019; Vasavada et al., 1993).

7. Conclusions

Our objective in this study was to obtain new constraints on Mars' paleopressure history 3.8–4 Ga. To do this, we compared crater populations preserved in ancient sedimentary rocks in Mawrth Vallis (> 4 Ga & 3.8 ± 0.2

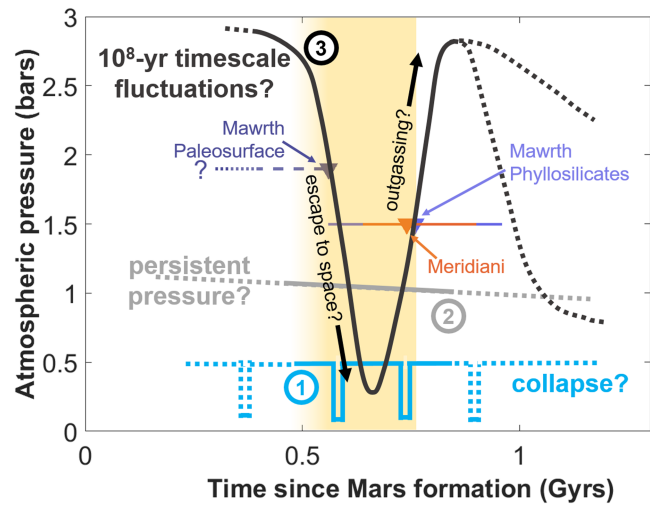


Figure 13. Schematic illustrating 3 atmospheric pressure histories for Mars between ~ 4 Ga and 3.8 ± 0.2 Ga (yellow area). Triangles with age uncertainties are our new upper bounds on continuous atmospheric pressure (dark purple at 4 Ga - Mawrth paleosurface, light purple - Mawrth phyllosilicates, orange - Meridiani). The blue box-car function illustrates a <0.5 bar atmosphere that undergoes periods of collapse. The grey line illustrates an atmosphere that remains continuously at our constant pressure upper limits. The black curve illustrates several bar of atmospheric pressure changes due to changes in atmospheric sources and sinks. Dotted lines/curves indicate time that is not covered by our new results.

Ga) and Meridiani Planum ($3.82^{+0.10}_{-0.18}$ Ga) to predict crater populations generated from a forward model of atmosphere-impactor interactions. At 3.8 ± 0.2 Ga, our results are consistent with two end-member cases:

1. Continuous paleo-atmospheric pressure of 6 mbar during the period of crater accumulation. Observed crater populations accumulated over a minimum of 10^4 years (Mawrth phyllosilicates site) to 10^5 years (Meridiani).
2. Continuous paleo-atmospheric pressure of 1.5 bar during the period of crater accumulation. Observed crater populations accumulated over a minimum of 10^5 years (Mawrth phyllosilicates site) to 10^6 years (Meridiani).

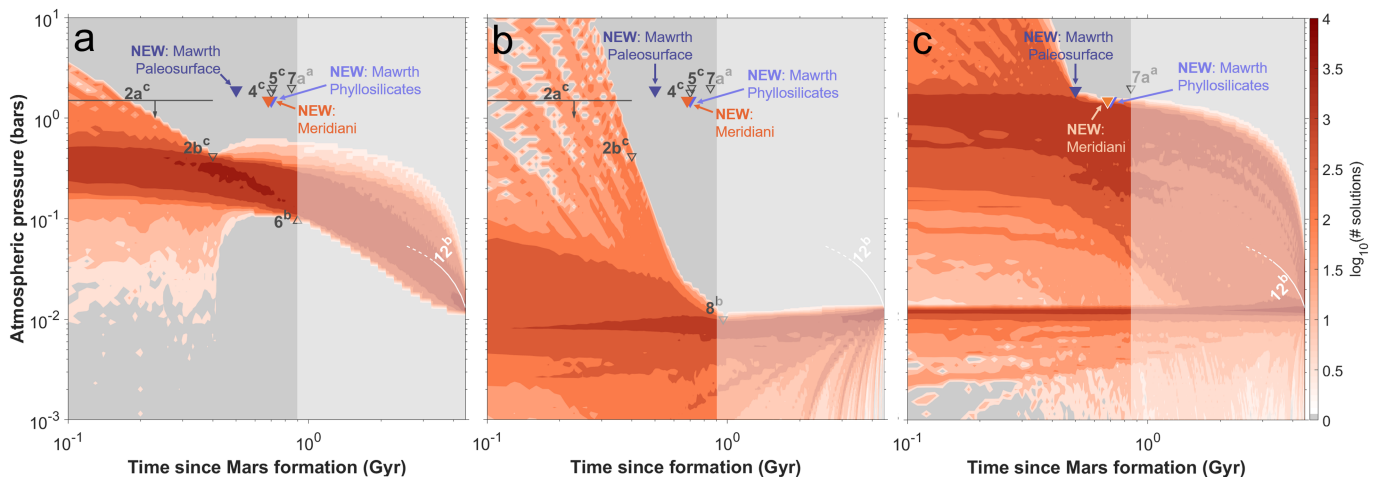


Figure 14. Solution density contour plots of pressure histories allowed by existing paleopressure estimates from our basic, 2-component atmospheric evolution model. All possible source/sink combinations are superimposed on one another for 10,000 possible combinations of k_{1-4} . Dark gray areas do not match data. Washed out (light gray) region indicates area of graph from ~ 3.6 Ga to present where no paleopressure estimates exist and solutions are not well constrained. $\log_{10}(\# \text{ solutions}) = 4$ indicates that 10,000 possible solutions pass through point. (a) lower bound on paleo-atmospheric pressure comes from Manga et al. (2012) (6^b), pressure calculated from bomb sag structure at Home Plate at $3.66^{+0.44}_{-0.31}$ Ga and (b) Lapotre et al. (2016) (8^b), pressure calculated from large wind ripples in the Burns formation as the maximum constraint $/3.6 \pm 0.1$ Ga, respectively (c) only paleopressure constraints from ancient crater size frequency distributions (methods used in this paper). 12^b is the upper limit on MAVEN escape rate extrapolated backwards through time. This is only enforced as a constraint at $t = 4.56$ Gyr (i.e., Neumann boundary condition at present day). All other constraints are as for Figure 7.

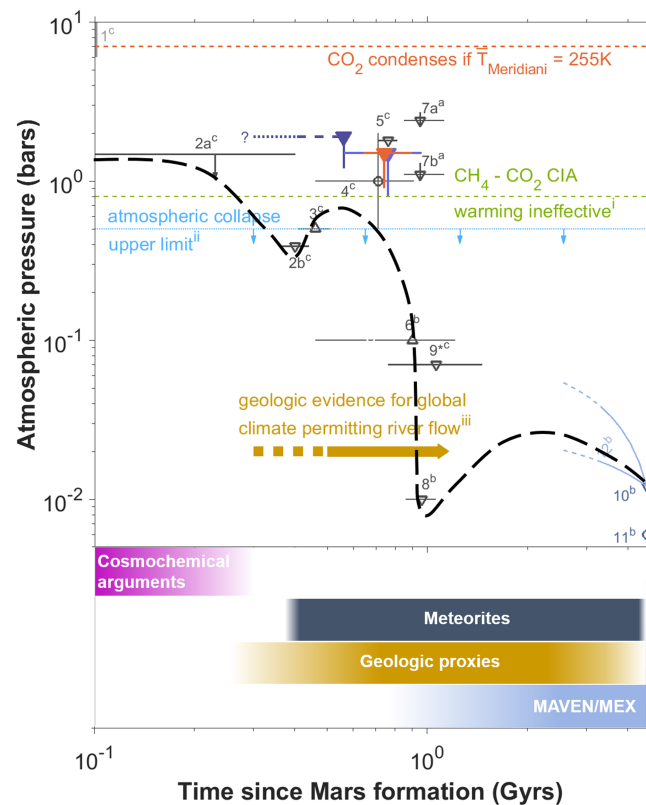


Figure 15. Schematic illustration of one possible pressure history for Mars that satisfies all existing paleopressure constraints. Superscripts: (a) - constraints from small, ancient, embedded craters, (b) - constraints from remote sensing, (c) constraints from all other techniques (meteorite analyses, modelling, etc.). Upward (downward)-pointing triangles - lower (upper) bounds. Circles - estimates of absolute atmospheric pressure or direct measurements. Downward arrows from a horizontal line - pressure must have been below the given value for the entire time interval. Numbers for paleopressure constraints are as for Figure 7. i) CH_4 - CO_2 collision-induced absorption warming is ineffective below atmospheric pressures of 0.8 bar (Turbet, Tran, et al., 2019), ii) from GCMs, the upper bound on atmospheric pressure for atmospheric collapse into CO_2 ice caps to occur is 0.5 bar (Forget et al., 2013; Soto et al., 2015), iii) the last year that widespread fluvial activity on Mars was permitted by global climate was <3.4 Ga (Kite, 2019) (additionally, there is evidence for <1 Ga Amazonian supraglacial channels Dickson et al., 2009 and late (<2 Ga) alluvial fan activity in Gale Crater Grant & Wilson, 2019).

Our measured CSFDs indicate that paleoatmospheric pressure on Mars >4 Ga was either continuously below 1.9 ± 0.1 bar or varied between pressures above and below this upper limit on continuous atmospheric pressure. Therefore, our new data are consistent with either continuously low (< 1.5 bar) atmospheric pressures or alternatively variations of several bar in atmospheric pressure due to the changing balance between atmospheric sources and sinks. Thus, a diverse range of paleopressure histories for Mars in the interval $4\text{--}3.8 \pm 0.2$ Ga are all consistent with our new data (Figure 13). Source and sink processes leave imprints on Mars' geologic record that we can potentially compare to the timing of our measured crater populations to assess the feasibility of different atmospheric pressure histories. The feasibility of pressure oscillations with amplitudes of several bar between pressures above and below our upper limits on continuous pressure due to changes in processes such as outgassing, impacts, escape to space, and carbonate formation from $4\text{--} \pm 0.2$ Ga could be constrained through better dating of our ancient embedded crater counting sites (e.g., through sample return missions), improved understanding of the extent and duration of carbonate deposition on Mars, and better relative and absolute age-dating for events such as the growth of Tharsis.

Our results agree with existing paleopressure constraints, including sedimentary features such as the Home Plate bomb sag (Manga et al., 2012) (6^b) and modeling studies based on mineral stability and carbonate deposition (Hu et al., 2015(5^c), van Berk et al., 2012 (4^c), where superscripts refer to Figure 7). We also demonstrate that paleopressure estimates for a single site are representative of global zero-elevation

corrected surface pressure. However, due to the effects of sedimentation and erosion on observed crater populations, our results give conservative (high) upper bounds.

We combine our new paleopressure upper limits with existing constraints, and compare the combination to the output from a basic model of Mars atmospheric pressure evolution. Our process-agnostic, 2-component model of sources and sinks of volatiles (CO_2) to the atmosphere is very strongly sensitive to constraints that give lower bounds on atmospheric pressure (Figure 14). Additionally, our method cannot constrain rapid changes in atmospheric pressure due to collapse (Figure 15). Thus, more paleopressure constraints for Mars are needed, particularly between 3.6 Ga and present where the only existing constraints are the measured MAVEN escape rate and Mars' existing surface and atmospheric CO_2 reservoirs. The greatest density of possible solutions for Mars' atmospheric pressure history suggest atmospheric pressures on Early Mars between 0.01 and 1 bar. This agrees with the earliest upper bounds on atmospheric pressure as modeled using data from ALH84001 (Cassata et al., 2012) (2a^c & 2b^c, Figure 7). This range is significantly lower than our new paleopressure upper bounds.

Acknowledgments

J. Sneed produced the HiRISE DTMs using the pipeline of Mayer and Kite (2016). The contributions of J.-P. W. were funded by a NASA Solar System Workings grant 80NSSC18K0010. We acknowledge the use of University of Chicago Research Computing Center resources. Grants: NASA NNX16AJ38G (E.S.K.). DTMs in Table 1 can be found at www.uahirise.org/dtm/ unless stated otherwise. Crater counts and MATLAB scripts used for fitting procedure are available at github.com/aowarren/crater_counts. The authors would like to thank the three anonymous reviewers for their constructive comments and suggestions. Author contributions: A.O.W. and E.S.K. designed the research, which was conceived by E.S.K. A.O.W. carried out research. A.O.W. wrote the paper. J.-P.W. wrote the forward model of impactor-atmosphere interactions. B.H. contributed CRISM-based mineralogic maps. All authors contributed to editing the paper, the revisions, and concomitant additional work.

References

- Aharonson, O., Schorghofer, N., & Gerstell, M. F. (2003). Slope streak formation and dust deposition rates on Mars. *Journal of Geophysical Research*, 108(E12), 5138. <https://doi.org/10.1029/2003JE002123>
- Ansan, V., & Mangold, N. (2006). New observations of Warrego valles, mars: Evidence for precipitation and surface runoff. *Planetary and Space Science*, 54(3), 219–242.
- Ayres, T. (1997). Evolution of the solar ionizing flux. *Journal of Geophysical Research*, 102, 1641–1651.
- Bahcall, J. N., Pinsonneault, M. H., & Basu, S. (2001). Solar Models: Current epoch and time dependences, neutrinos, and helioseismological properties. *The Astrophysical Journal*, 555(2), 990–1012.
- Baker (2017). Basalt weathering and the volatile budget of early Mars, In *Lunar and Planetary Science Conference* (Vol. 2014, pp. 3081). Arizona: LPI Contribution.
- Batalha, N., Domagal-Goldman, S. D., Ramirez, R., & Kasting, J. F. (2015). Testing the early Mars H_2 - CO_2 greenhouse hypothesis with a 1-D photochemical model. *Icarus*, 258, 337–349.
- Biersen, C. J., Phillips, R. J., Smith, I. B., Wood, S. E., Putzig, N. E., Nunes, D., & Byrne, S. (2016). Stratigraphy and evolution of the buried CO_2 deposit in the Martian south polar cap. *Geophysical Research Letters*, 43, 4172–4179. <https://doi.org/10.1002/2016GL068457>
- Bishop, J. L., Dobre, E. Z. N., McKeown, N. K., Parente, M., Ehlmann, B. L., Michalski, J. R., et al. (2008). Phyllosilicate diversity and past aqueous activity Revealed at Mawrth Vallis, mars. *Science*, 321(5890), 830–833.
- Bishop, J. L., Fairén, A. G., Michalski, J. R., Gago-Duport, L., Baker, L. L., Velbel, M. A., et al. (2018). Surface clay formation during short-term warmer and wetter conditions on a largely cold ancient Mars. *Nature Astronomy*, 2(3), 206.
- Bishop, J. L., & Rampe, E. B. (2016). Evidence for a changing Martian climate from the mineralogy at Mawrth Vallis. *Earth and Planetary Science Letters*, 448, 42–48.
- Bland, P. A., & Artemieva, N. A. (2006). The rate of small impacts on Earth. *Meteoritics and Planetary Science*, 41(4), 607–631.
- Boslough, M. B. E., & Crawford, D. A. (2016). Low-altitude airbursts and the impact threat. *International Journal of Impact Engineering*, 35(12), 1441–1448.
- Brain, D. A., Bagenal, F., Ma, Y.-J., Nilsson, H., & Wieser, G. S. (2016). Atmospheric escape from unmagnetized bodies. *Journal of Geophysical Research: Planets*, 121, 2364–2385. <https://doi.org/10.1002/2016JE005162>
- Bristow, T. F., Haberle, R. M., Blake, D. F., Marais, D. J. D., Eigenbrode, J. L., Fairén, A. G., et al. (2017). Low Hesperian pCO_2 constrained from in situ mineralogical analysis at Gale Crater, Mars. *Proceedings of the National Academy of Sciences*, 114(9), 2166–2170.
- Brown, P., Spalding, R. E., ReVelle, D. O., Tagliaferri, E., & Worden, S. P. (2002). The flux of small near-Earth objects colliding with the Earth. *Nature*, 420(6913), 294.
- Bryson, C. E., Cazcarra, V., & Levenson, L. L. (1974). Sublimation rates and vapor pressures of water, carbon dioxide, nitrous oxide, and xenon. *Journal of Chemical & Engineering Data*, 19(2), 107–110.
- Buratti, B. J., Bauer, J. M., Hicks, M. D., Hillier, J. K., Verbiscer, A., Hammel, H., et al. (2011). Photometry of Triton 1992-2004: Surface volatile transport and discovery of a remarkable opposition surge. *Icarus*, 212, 835–846.
- Cassata, W. S., Shuster, D. L., Renne, P. R., & Weiss, B. P. (2012). Trapped Ar isotopes in meteorite ALH 84001 indicate Mars did not have a thick ancient atmosphere. *Icarus*, 221(1), 461–465.
- Cepilecha, Z., Borovcka, J., Elford, W. G., ReVelle, D. O., Hawkes, R. L., Porubcan, V., & Simek, M. (1998). Meteor Phenomena and Bodies. *Space Science Reviews*, 84(3), 327–471.
- Chappelow, J. E., & Sharpton, V. L. (2012). Influences of atmospheric variations on Mars's record of small craters. *Icarus*, 178(1), 40–55.
- Chassefière, E., & Leblanc, F. (2004). Mars atmospheric escape and evolution: Interaction with the solar wind. *Planetary and Space Science*, 52, 1039–1058.
- Chassefière, E., Leblanc, F., & Langlais, B. (2007). The combined effects of escape and magnetic field histories at Mars. *Planetary and Space Science*, 55(3), 343–357.
- Citron, R. I., Manga, M., & Hemingway, D. J. (2018). Timing of oceans on Mars from shoreline deformation. *Nature*, 555(7698), 643–646.
- Costa, F., Dohmen, R., & Chakraborty, S. (2008). Time scales of magmatic processes from modeling the zoning patterns of crystals. *Reviews in Mineralogy and Geochemistry*, 69, 545–594.
- Craddock, R. A., Maxwell, T. A., & Howard, A. D. (1997). Crater morphometry and modification in the Sinus Sabaeus and Margaritifer Sinus regions of Mars. *Journal of Geophysical Research*, 102(E6), 13,321–13,340.
- Davis, P. (1993). Meteoroid Impacts as Seismic Sources on Mars. *Icarus*, 105(2), 469–478.
- Davis, J., Gupta, S., Balme, M., Grindrod, P., Fawdon, P., Dickeson, Z. I., & Williams, R. (2016). A diverse array of fluvial depositional systems in Arabia Terra: Evidence for mid-Noachian to Early Hesperian Rivers on Mars. *Journal of Geophysical Research: Planets*, 124, 1913–1934. <https://doi.org/10.1029/2019JE005976>

- di Achille, G., & Hynek, B. M. (2010). Ancient ocean on Mars supported by global distribution of deltas and valleys. *Nature Geoscience*, 3, 459–463.
- Dickson, J. L., Fassett, C. I., & Head, J. W. (2009). Amazonian-aged fluvial valley systems in a climatic microenvironment on Mars: Melting of ice deposits on the interior of Lyot Crater. *Geophysical Research Letters*, 36, L08201. <https://doi.org/10.1029/2009GL037472>
- Dong, C., Lee, Y., Ma, Y., Lingam, M., Bougher, S., Luhmann, J., et al. (2018). Modeling Martian atmospheric losses over time: Implications for exoplanetary climate evolution and habitability. *The Astrophysical Journal*, 859(1), L14.
- Doran, P., Lyons, P., & McKnight, D. (2010). *Antarctic deserts and other cold dry environments: Astrobiological analogs*. Cambridge: Cambridge University Press.
- Dorren, D., & Guinan, E. F. (1994). HD 129333: the Sun in its infancy. *The Astrophysical Journal*, 428, 805–818.
- Fassett, C. I., & Head, J. W. (2005). Fluvial sedimentary deposits on Mars: Ancient deltas in a crater lake in the Nili Fossae region. *Geophysical Research Letters*, 32, L14201. <https://doi.org/10.1029/2005GL023456>
- Fastook, J. L., & Head, J. W. (2015). Glaciation in the Late Noachian Icy highlands: Ice accumulation, distribution, flow rates, basal melting, and top-down melting rates and patterns. *Planetary and Space Science*, 106, 82–98.
- Fernández-Fassnacht, E., & Rio, F. D. (1984). The vapour pressure of CO₂ from 194 to 243 K. *The Journal of Chemical Thermodynamics*, 16(5), 469–474.
- Folco, L., Di Martino, M., El Barkooky, A., D'Orazio, M., Lethy, A., Urbini, S., et al. (2011). Kamil Crater (Egypt): Ground truth for small-scale meteorite impacts on Earth. *Geology*, 39(2), 179–182.
- Forget, F., Wordsworth, R., Millour, E., Madeleine, J.-B., Kerber, L., Leconte, J., et al. (2013). 3D modelling of the early martian climate under a denser CO₂ atmosphere: Temperatures and CO₂ ice clouds. *Icarus*, 222(1), 81–99.
- Glotch, T. D., & Rogers, A. D. (2013). Evidence for magma-carbonate interaction beneath Syrtis Major, Mars. *Journal of Geophysical Research: Planets*, 118, 126–137. <https://doi.org/10.1029/2012JE004230>
- Gough, D. O. (1981). Solar interior structure and luminosity variations. In V. Domingo (Ed.), *Physics of Solar Variations* (Vol. 74, pp. 21–34). Dordrecht: Springer.
- Grant, J. A., & Schultz, P. H. (1993). Degradation of selected terrestrial and Martian impact craters. *Journal of Geophysical Research*, 98(E6), 11,025–11,042.
- Grant, J. A., & Wilson, S. A. (2019). Evidence for late alluvial activity in Gale Crater, mars. *Geophysical Research Letters*, 46, 7287–7294. <https://doi.org/10.1029/2019GL083444>
- Greeley, R., & Schneid, B. (1991). Magma generation on Mars — Amounts, rates, and comparisons with earth, moon, and Venus. *Science*, 254, 996–998.
- Grotzinger, J. P., & Milliken, R. E. (2012). The sedimentary rock record of Mars: Distribution, origins, and global stratigraphy. *Sedimentary Geology of Mars* (Vol. 102, pp. 1–48). Tulsa, OK: SEPM Special Publication.
- Grotzinger, J. P., Sumner, D. Y., Kah, L. C., Stack, K., Gupta, S., Edgar, L., et al. (2014). A Habitable fluvio-lacustrine environment at Yellowknife bay, gale crater, Mars. *Science*, 343(6169), 1242777.
- Haberle, R. (1998). Early Mars Climate Models. *Journal of Geophysical Research*, 103(E12), 28,467–28,479.
- Haberle, R. M., Tyler, D., McKay, C. P., & Davis, W. L. (1994). A model for the evolution of CO₂ on Mars. *Icarus*, 109(1), 102–120.
- Halevy, I., & Head, J. W. (2014). Episodic warming of early Mars by punctuated volcanism. *Nature Geoscience*, 7(12), 865–868.
- Hauck, S. A., & Phillips, R. J. (2002). Thermal and crustal evolution of Mars. *Journal of Geophysical Research*, 107(E7), 5052. <https://doi.org/10.1029/2001JE001801>
- Head, J. W., & Marchant, D. R. (2014). The climate history of early Mars: Insights from the Antarctic McMurdo Dry Valleys hydrologic system. *Antarctic Science*, 26(6), 774–800.
- Hecht, M. (2002). Metastability of Liquid Water on Mars. *Icarus*, 156(2), 373–386.
- Hills, J. G., & Goda, M. P. (1993). The fragmentation of small asteroids in the atmosphere. *The Astronomical Journal*, 105(3), 1114–1144.
- Holsapple, K. (1993). The scaling of impact processes in planetary sciences. *Annual Review of Earth and Planetary Sciences*, 21, 333–373.
- Hu, R., Kass, D. M., Ehlmann, B. L., & Yung, Y. L. (2015). Tracing the fate of carbon and the atmospheric evolution of Mars. *Nature Communications*, 6, 10003.
- Hynek, B. M., Beach, M., & Hoke, M. R. T. (2010). Updated global map of Martian valley networks and implications for climate and hydrologic processes. *Journal of Geophysical Research*, 115, E09008. <https://doi.org/10.1029/2009JE003548>
- Hynek, B., & di Achille, G. (2017). Geologic map of Meridiani Planum, Mars, 3356.
- Ivanov, B. (2001). Mars/moon cratering rate ratio estimates. *Chronology and Evolution of Mars*, 96, 87–104.
- Jakosky, B. (2019). The CO₂ inventory on Mars. *Planetary and Space Science*, 175(1), 52–59.
- Jakosky, B. M., Brain, D., Chaffin, M., Curry, S., Deighan, J., Grebowsky, J., et al. (2018). Loss of the Martian atmosphere to space: Present-day loss rates determined from MAVEN observations and integrated loss through time. *Icarus*, 315, 146–157.
- Jakosky, B. M., & Phillips, R. J. (2001). Mars' volatile and climate history. *Nature*, 412(6843), 237.
- Jerolmack, D. J., & Sadler, P. (2007). Transience and persistence in the depositional record of continental margins. *Journal of Geophysical Research*, 112, F03S13. <https://doi.org/10.1029/2006JF000555>
- Jessup, K. L., Spencer, J. R., Ballester, G. E., Howell, R. R., Roesler, F., Vigel, M., & Yelle, R. (2004). The atmospheric signature of Io's Prometheus plume and anti-jovian hemisphere: Evidence for a sublimation atmosphere. *Icarus*, 169, 197–215.
- Kite, E. (2019). Geologic Constraints on Early Mars climate. *Space Science Reviews*, 215(1), 10.
- Kite, E. S., Gao, P., Goldblatt, C., Mischna, M. A., Mayer, D. P., & Yung, Y. L. (2017). Methane bursts as a trigger for intermittent lake-forming climates on post-Noachian Mars. *Nature Geoscience*, 10(10), 737–740.
- Kite, E. S., Lucas, A., & Fassett, C. I. (2013). Pacing early Mars river activity: Embedded craters in the Aeolis Dorsa region imply river activity spanned (1–20)Myr. *Icarus*, 225(1), 850–855.
- Kite, E. S., Williams, J.-P., Lucas, A., & Aharonson, O. (2014). Low palaeopressure of the martian atmosphere estimated from the size distribution of ancient craters. *Nature Geoscience*, 7, 335–339.
- Korycansky, D. G., Zahnle, K. J., & Atmospheric impacts, fragmentation (2004). *Icarus*, 169(2), 287–299.
- Korycansky, D. G., Zahnle, K. J., & Modeling crater populations on V, enusandTitan (2005). *Planetary and Space Science*, 53(7), 695–710.
- Kreslavsky, M. A., & Head, J. W. (2005). Mars at very low obliquity: Atmospheric collapse and the fate of volatiles. *Geophysical Research Letters*, 32, L12202. <https://doi.org/10.1029/2005GL022645>
- Kurahashi-Nakamura, T., & Tajika, E. (2006). Atmospheric collapse and transport of carbon dioxide into the subsurface on early Mars. *Geophysical Research Letters*, 33, L18205. <https://doi.org/10.1029/2006GL027170>
- Kurokawa, H., Kurosawa, K., & Usui, T. (2018). A lower limit of atmospheric pressure on early Mars inferred from nitrogen and argon isotopic compositions. *Icarus*, 299, 443–459.

- Lammer, H., Chassefière, E., Karatekin, Ö., Morschhauser, A., Niles, P. B., Mousis, O., et al. (2013). Outgassing History and Escape of the Martian Atmosphere and Water Inventory. *Space Science Reviews*, 174(1), 113–154.
- Lapotre, M. G. A., Ewing, R. C., Lamb, M. P., Fischer, W. W., Grotzinger, J. P., Rubin, D. M., et al. (2016). Large wind ripples on Mars: A record of atmospheric evolution. *Science*, 353, 55–58.
- Laskar, J., Correia, A. C. M., Gastineau, M., Joutel, F., Levrard, B., & Robutel, P. (2004). Long term evolution and chaotic diffusion of the insolation quantities of Mars. *Icarus*, 170(2), 343–364.
- Lillis, R. J., Brain, D. A., Bougher, S. W., Leblanc, F., Luhmann, J. G., Jakosky, B. M., et al. (2015). Characterizing atmospheric escape from Mars today and through time, with MAVEN. *Space Science Reviews*, 195(1), 357–422.
- Loizeau, D., Mangold, N., Poulet, F., Ansan, V., Hauber, E., Bibring, J.-P., et al. (2010). Stratigraphy in the Mawrth Vallis region through OMEGA, HRSC color imagery and DTM. *Icarus*, 205, 396–418.
- Loizeau, D., Mangold, N., Poulet, F., Bibring, J., Gendrin, A., Ansan, V., et al. (2007). Phyllosilicates in the Mawrth Vallis region of Mars. *Journal of Geophysical Research*, 112, E08S08. <https://doi.org/10.1029/2006JE002877>
- Loizeau, D., Werner, S. C., Mangold, N., Bibring, J.-P., & Vago, J. L. (2012). Chronology of deposition and alteration in the Mawrth Vallis region, Mars. *Planetary and Space Science*, 72, 31–43.
- Lyne, J. E., Tauber, M., & Fought, R. (1996). An analytical model of the atmospheric entry of large meteors and its application to the Tunguska Event. *Journal of Geophysical Research*, 101(E10), 23,207–23,212.
- Malin, M. C., & Edgett, K. S. (2000). Sedimentary Rocks of Early Mars. *Science*, 290(5498), 1927–1937.
- Manga, M., Patel, A., Dufek, J., & Kite, E. S. (2012). Wet surface and dense atmosphere on early Mars suggested by the bomb sag at Home Plate, Mars. *Geophysical Research Letters*, 39, L01202. <https://doi.org/10.1029/2011GL050192>
- Mangold, N., Ansan, V., Masson, P., Quantin, C., & Neukum, G. (2008). Geomorphic study of fluvial landforms on the northern Valles Marineris plateau, Mars. *Journal of Geophysical Research*, 113, E08009. <https://doi.org/10.1029/2007JE002985>
- Mangold, N., Quantin, C., Ansan, V., Delacourt, C., & Allemand, P. (2004). Evidence for precipitation on Mars from dendritic valleys in the Valles Marineris Area. *Science*, 305(5680), 78–81.
- Manning, C. V., Bierson, C., Putzig, N. E., & McKay, C. P. (2019). The formation and stability of buried polar CO₂ deposits on Mars. *Icarus*, 317, 509–517.
- Marchant, D. R., & Head, J. W. (2007). Antarctic dry valleys: Microclimate zonation, variable geomorphic processes, and implications for assessing climate change on Mars. *Icarus*, 192(1), 187–222.
- Matson, D. L., Davies, A. G., Veeder, G. J., Rathbun, J. A., Johnson, T. V., & Castillo, J. C. (2006). Io: Loki Patera as a magma sea. *Journal of Geophysical Research*, 111, E09002. <https://doi.org/10.1029/2006JE002703>
- Mayer, D. P., & Kite, E. S. (2016). An integrated workflow for producing digital terrain models of Mars from CTX and hiRISE Stereo Data Using the NASA Ames Stereo Pipeline. *Lunar and Planetary Science Conference* (Vol. 47, pp. 1241). The Woodlands, Texas: LPI Contribution.
- McEwen, A. S., Preblich, B. S., Turtle, E. P., Artemieva, N. A., Golombek, M. P., Hurst, M., et al. (2005). The rayed crater Zunil and interpretations of small impact craters on Mars. *Icarus*, 176, 351–381.
- Melosh, H. (1981). Atmospheric breakup of terrestrial impactors, *Multi-ring basins: Formation and Evolution* (pp. 29–35). New York and Oxford: Pergamon Press.
- Michael, G. G. (2013). Planetary surface dating from crater size-frequency distribution measurements: Multiple resurfacing episodes and differential isochron fitting. *Icarus*, 226(1), 885–890.
- Michalski, J. R., Bibring, J.-P., Poulet, F., Loizeau, D., Mangold, N., Dobrea, E. N., et al. (2010). The Mawrth Vallis Region of Mars: A Potential Landing Site for the Mars Science Laboratory (MSL) Mission. *Astrobiology*, 10(7), 687–703.
- Moore, J. M., Howard, A. D., Dietrich, W. E., & Schenk, P. M. (2003). Martian layered fluvial deposits: Implications for Noachian climate scenarios. *Geophysical Research Letters*, 30(24), 2292. <https://doi.org/10.1029/2003GL019002>
- Morschhauser, A., Grott, M., & Breuer, D. (2011). Crustal recycling, mantle dehydration, and the thermal evolution of Mars. *Icarus*, 212, 541–558.
- Murphy, D. M., & Koop, T. (2005). Review of the vapour pressures of ice and supercooled water for atmospheric applications. *Quarterly Journal of the Royal Meteorological Society*, 131(608), 1539–1565.
- Nakamura, T., & Tajika, E. (2003). Climate change of Mars-like planets due to obliquity variations: implications for Mars. *Geophysical Research Letters*, 30(13), 1685. <https://doi.org/10.1029/2002GL016725>
- Nimmo, F., & Tanaka, K. (2005). Early crustal evolution of Mars. *Annual Review of Earth and Planetary Sciences*, 33, 133–161.
- Nininger, H. H., & Figgins, J. D. (1933). The excavation of a meteorite crater near haviland, kiowa county, Kansas. *Colorado Museum of Natural History, Proceedings*, 12(3), 9–15.
- Nuno, R. G., & Paige, D. A. (2019). Martian microcraters as evidence for obliquity-driven pressure variations, *Lunar and Planetary Science Conference* (Vol. 50, pp. 3096). The Woodlands, Texas: Lunar and Planetary Science Conference.
- Oehler, D. Z., & Allen, C. C. (2012). Giant polygons and mounds in the lowlands of Mars: Signatures of an ancient ocean? *Astrobiology*, 12, 601–615.
- Öpik, E. (1966). The Martian surface. *Science*, 15, 255–265.
- Passey, Q. R., & Melosh, H. J. (1980). Effects of atmospheric breakup on crater field formation. *Icarus*, 42(2), 211–233.
- Pepin, R. (1994). Evolution of the Martian Atmosphere. *Icarus*, 111(2), 289–304.
- Pham, L. B. S., & Karatekin, O. (2016). Scenarios of atmospheric mass evolution on Mars influenced by asteroid and comet impacts since the late Noachian. *Planetary and Space Science*, 125, 1–11.
- Phillips, R. J., Zuber, M. T., Solomon, S. C., Golombek, M. P., Jakosky, B. M., Banerdt, W. B., et al. (2001). Ancient geodynamics and global-scale hydrology on Mars. *Science*, 291(5513), 2587–2591.
- Podolak, M., Pollack, J. B., & Reynolds, R. T. (1988). Interactions of planetesimals with protoplanetary atmospheres. *Icarus*, 73(1), 163–179.
- Pollack, J. B., Kasting, J. F., Richardson, S. M., & Poliakov, K. (1987). The case for a wet, warm climate on early Mars. *Icarus*, 71(2), 203–224.
- Popova, O., Nemtchinov, I., & Hartmann, W. K. (2003). Bolides in the present and past martian atmosphere and effects on cratering processes. *Meteoritics & Planetary Science*, 38(6), 905–925.
- Putzig, N. E., Smith, I. B., Perry, M. R., Foss, F. J., Campbell, B., Phillips, R. J., & Poliakov, R. S. e. u. K. (1987). Three-dimensional radar imaging of structures and craters in the Martian polar caps. *Icarus*, 308, 138–147.
- Ramirez, R. (2017). A warmer and wetter solution for early Mars and the challenges with transient warming. *Icarus*, 297, 71–82.
- Ramirez, R. M., Kopparapu, R., Zuger, M. E., Robinson, T. D., Freedman, R., & Kasting, J. F. (2014). Warming early Mars with CO₂ and H₂. *Nature Geoscience*, 7, 59–63.
- Saito, H., & Kuramoto, K. (2017). Formation of a hybrid-type proto-atmosphere on Mars accreting in the solar nebula. *Monthly Notices of the Royal Astronomical Society*, 475, 1274–1287.

- Sakuraba, H., Kurokawa, H., & Genda, H. (2019). Impact degassing and atmospheric erosion on Venus, Earth, and Mars during the late accretion. *Icarus*, 317, 48–58.
- Schlichting, H. E., Sari, R., & Yalinewich, A. (2015). Atmospheric mass loss during planet formation: The importance of planetesimal impacts. *Icarus*, 247, 81–94.
- Segura, T. L., McKay, C. P., & Toon, O. B. (2012). An impact-induced, stable, runaway climate on Mars. *Icarus*, 220, 144–148.
- Shoemaker, E. M., Macdonald, F. A., & Shoemaker, C. S. (2005). Geology of five small Australian impact craters. *Australian Journal of Earth Sciences*, 52(4–5), 529–544.
- Slipski, M., & Jakosky, B. M. (2016). Argon isotopes as tracers for martian atmospheric loss. *Icarus*, 272, 212–227.
- Smith, M. R., Gillespie, A. R., & Montgomery, D. R. (2008). Effect of obliteration on crater-count chronologies for Martian surfaces. *Geophysical Research Letters*, 35, L10202. <https://doi.org/10.1029/2008GL033538>
- Soto, A., Mischna, M., Schneider, T., Lee, C., & Richardson, M. (2015). Martian atmospheric collapse: Idealized GCM studies. *Icarus*, 250, 553–569.
- Stanley, B. D., Hirschmann, M. M., & Withers, A. C. (2011). CO₂ solubility in Martian basalts and Martian atmospheric evolution. *Geochimica et Cosmochimica Acta*, 75(20), 5987–6003.
- Steakley, K., Murphy, J., Kahre, M., Haberle, R., & Kling, A. (2019). Testing the impact heating hypothesis for early Mars with a 3-D global climate model. *Icarus*, 330(15), 169–188.
- Stephens, S. K., & Stevenson, D. J. (1990). Dry carbonate formation on Mars: A plausible sink for an early dense CO₂ atmosphere? *Lunar and Planetary Science Conference* (Vol. 21, pp. 56). Houston, TX: Lunar and Planetary Science Conference.
- Strom, R. G., Malhotra, R., Ito, T., Yoshida, F., & Kring, D. A. (2005). The Origin of planetary impactors in the inner solar system. *Science*, 309(5742), 1847–1850.
- Strom, R. G., Malhotra, R., Xiao, Z. Y., Ito, T., Yoshida, F., & Ostrach, L. R. (2015). The inner solar system cratering record and the evolution of impactor populations. *Astronomy & Astrophysics*, 15, 407–434.
- Svetsov, V. V., Nemtchinov, I. V., & Teretev, A. V. (1995). Disintegration of large meteoroids in Earth's atmosphere: Theoretical models. *Icarus*, 116(1), 131–153.
- Tanaka, K. L., Skinner, J. A., Hare, T. M., Joyal, T., & Wenker, A. (2003). Resurfacing history of the northern plains of Mars based on geologic mapping of Mars Global Surveyor data. *Journal of Geophysical Research*, 108(E4), 8043. <https://doi.org/10.1029/2002JE001908>
- Tancredi, G., Ishitsuka, J., Schultz, P. H., Harris, R. S., Brown, P., Revelle, D. O., et al. (2009). A meteorite crater on Earth, formed on September 15, 2007: The Carancas hypervelocity impact. *Meteoritics & Planetary Science*, 44(12), 1967–1984.
- Tauber, M. E., & Kirk, D. B. (1976). Impact craters on Venus. *Icarus*, 28(3), 351–357.
- Tian, F., Kasting, J. F., & Solomon, S. C. (2009). Thermal escape of carbon from the early Martian atmosphere. *Geophysical Research Letters*, 36, L02205. <https://doi.org/10.1029/2008GL036513>
- Tosca, N. J., Ahmed, I. A. M., Tutolo, B. M., Ashpitel, A., & Hurowitz, J. A. (2018). Magnetite authigenesis and the warming of early Mars. *Nature Geoscience*, 11(9), 635.
- Touma, J., & Wisdom, J. (1993). The Chaotic Obliquity of Mars. *Science*, 259(5099), 1294–1297.
- Trenberth, K. E., Christy, J. R., & Olson, J. G. (1987). Global atmospheric mass, surface pressure, and water vapor variations. *Journal of Geophysical Research*, 92(D12), 14815.
- Tu, L., Johnstone, C. P., Güdel, M., & Lammer, H. (2015). The extreme ultraviolet and X-ray Sun in Time: High-energy evolutionary tracks of a solar-like star. *Astronomy & Astrophysics*, 557(L3).
- Turbet, M., Gillmann, C., Forget, F., Baudin, B., Palumbo, A., Head, J., & Karatekin, O. (2019). The environmental effects of very large bolide impacts on early Mars explored with a hierarchy of numerical models.
- Turbet, M., Tran, H., Pirali, O., Forget, F., Boulet, C., & Hartmann, J.-M. (2019). Far infrared measurements of absorptions by CH₄+CO₂ and H₂+CO₂ mixtures and implications for greenhouse warming on early Mars. *Icarus*, 321, 189–199.
- van Berk, W., Fu, Y., & Ilger, J. (2012). Reproducing early Martian atmospheric carbon dioxide partial pressure by modeling the formation of Mg-Fe-Ca carbonate identified in the COMANCHE rock outcrops on Mars. *Journal of Geophysical Research*, 117, E10008. <https://doi.org/10.1029/2012JE004173>
- Vasavada, A. R., Milavec, T. J., & Paige, D. A. (1993). Microcraters on Mars: Evidence for past climate variations. *Journal of Geophysical Research*, 98(E2), 3469–3476.
- Watters, W. A., Geiger, L. M., Fendro, M., & Gibson, R. (2015). Morphometry of small recent impact craters on Mars: Size and terrain dependence, short-term modification. *Journal of Geophysical Research: Planets*, 120, 226–254. <https://doi.org/10.1002/2014JE004630>
- Williams, J.-P., Pathare, A. V., & Aharonson, O. (2014). The production of small primary craters on Mars and the Moon. *Icarus*, 235, 23–36.
- Williams, J.-P., van der Bogert, C. H., Pathare, A. V., Michael, G. G., Kirchoff, M. R., & Hiesinger, H. (2017). Dating very young planetary surfaces from crater statistics: A review of issues and challenges. *Meteoritics & Planetary Science*, 53, 554–582.
- Wordsworth, R., Forget, F., Millour, E., Head, J., Madeleine, J.-B., & Charnay, B. (2013). Global modelling of the early Martian climate under a denser CO₂ atmosphere: Water cycle and ice evolution. *Icarus*, 222(1), 1–19. arXiv: 1207.3993.
- Wordsworth, R., Kalugina, Y., Lokshantov, S., Vigan, A., Ehlmann, B., Head, J., et al. (2017). Transient reducing greenhouse warming on early Mars. *Geophysical Research Letters*, 44, 665–671. <https://doi.org/10.1002/2016GL071766>
- Wordsworth, R. D., Kerber, L., Pierrehumbert, R. T., Forget, F., & Head, J. W. (2015). Comparison of “warm and wet” and “cold and icy” scenarios for early Mars in a 3-D climate model. *Journal of Geophysical Research: Planets*, 120, 1201–1219. <https://doi.org/10.1002/2015JE004787>
- Wray, J. J., Murchie, S. L., Bishop, J. L., Ehlmann, B. L., Milliken, R. E., Wilhelm, M. B., et al. (2016). Orbital evidence for more widespread carbonate-bearing rocks on Mars. *Journal of Geophysical Research: Planets*, 121, 652–677. <https://doi.org/10.1002/2015JE004972>